

The ALMA-QUARKS survey: – I. Survey description and data reduction

Xunchuan Liu (刘训川)¹, Tie Liu¹, Lei Zhu², Guido Garay³, Hong-Li Liu⁴, Paul Goldsmith⁵, Neal Evans⁶, Kee-Tae Kim⁷, Sheng-Yuan Liu⁸, Fengwei Xu^{9,10}, Xing Lu¹, Anandmayee Tej¹¹, Xiaofeng Mai¹, Leonardo Bronfman³, Shanghuo Li¹², Diego Mardones³, Amelia Stutz¹³, Ken'ichi Tatematsu¹⁴, Ke Wang⁹, Qizhou Zhang¹⁵, Sheng-Li Qin⁴, Jianwen Zhou¹⁶, Qiuyi Luo^{1,17}, Siju Zhang⁹, Yu Cheng¹⁸, Jinhua He^{19,2,3}, Qilao Gu¹, Ziyang Li^{1,4}, Zhenying Zhang^{1,4}, Suinan Zhang¹, Anindya Saha¹¹, Lokesh Dewangan²⁰, Patricio Sanhueza^{18,21}, Zhiqiang Shen¹,

¹ Shanghai Astronomical Observatory, Chinese Academy of Sciences, Shanghai 200030, PR China;

liuxunchuan@shao.ac.cn, liutie@shao.ac.cn

² Chinese Academy of Sciences South America Center for Astronomy, National Astronomical Observatories, Chinese Academy of Sciences, Beijing, 100101, PR China; *lzhupku@gmail.com*

³ Departamento de Astronomía, Universidad de Chile, Las Condes, 7591245 Santiago, Chile; *guido@das.uchile.cl*

⁴ School of Physics and Astronomy, Yunnan University, Kunming, 650091, PR China; *honglilium2012@gmail.com*

⁵ Jet Propulsion Laboratory, California Institute of Technology, 4800 Oak Grove Drive, Pasadena CA 91109, USA

⁶ Department of Astronomy, The University of Texas at Austin, Texas 78712-1205, USA

⁷ Korea Astronomy and Space Science Institute, 776 Daedeokdae-ro, Yuseong-gu, Daejeon 34055, Republic of Korea

⁸ Institute of Astronomy and Astrophysics, Academia Sinica, Roosevelt Road, Taipei 10617, Taiwan (R.O.C)

⁹ Kavli Institute for Astronomy and Astrophysics, Peking University, Haidian District, Beijing 100871, PR China

¹⁰ Department of Astronomy, School of Physics, Peking University, Beijing 100871, PR China

¹¹ Indian Institute of Space Science and Technology, Thiruvananthapuram 695 547, Kerala, India

¹² Max Planck Institute for Astronomy, Königstuhl 17, D-69117 Heidelberg, Germany

¹³ Departamento de Astronomía, Universidad de Concepción, Casilla 160-C, Concepción, Chile

¹⁴ Nobeyama Radio Observatory, National Astronomical Observatory of Japan, National Institutes of Natural Sciences, 462-2 Nobeyama, Minamimaki, Minamisaku, Nagano 384-1305, Japan

¹⁵ Center for Astrophysics | Harvard & Smithsonian, 60 Garden Street, Cambridge, MA 02138, USA

¹⁶ Max-Planck-Institut für Radioastronomie, Auf dem Hügel 69, 53125 Bonn, Germany

¹⁷ School of Astronomy and Space Sciences, University of Chinese Academy of Sciences, Beijing 100049, PR China

¹⁸ National Astronomical Observatory of Japan, 2-21-1 Osawa, Mitaka, Tokyo, 181-8588, Japan

¹⁹ Yunnan Observatories, Chinese Academy of Sciences, Kunming, 650216, Yunnan, PR China

²⁰ Physical Research Laboratory, Navrangpura, Ahmedabad-380 009, India

²¹ GUAS Astronomical Science Program, SOKENDAI, 2-21-1 Osawa, Mitaka, Tokyo 181-8588, Japan

Received 20XX Month Day; accepted 20XX Month Day

Abstract This paper presents an overview of the QUARKS survey, which stands for ‘Querying Underlying mechanisms of massive star formation with ALMA-Resolved gas Kinematics and Structures’. The QUARKS survey is observing 139 massive clumps covered by 156 pointings at ALMA Band 6 ($\lambda \sim 1.3$ mm). In conjunction with data obtained from the ALMA-ATOMS survey at Band 3 ($\lambda \sim 3$ mm), QUARKS aims to carry out an unbiased statistical investigation of massive star formation process within protoclusters down to a scale of 1000 au. This overview paper describes the observations and data reduction of the QUARKS survey, and gives a first look at an exemplar source, the mini-starburst Sgr B2(M). The wide-bandwidth (7.5 GHz) and high-angular-resolution ($\sim 0.3''$) observations of the QUARKS survey allow to resolve much more compact cores than could be done by the ATOMS survey, and to detect previously unrevealed fainter filamentary structures. The spectral windows cover transitions of species including CO, SO, N_2D^+ , SiO, $H_{30}\alpha$, H_2CO , CH_3CN and many other complex organic molecules, tracing gas components with different temperatures and spatial extents. QUARKS aims to deepen our understanding of several scientific topics of massive star formation, such as the mass transport within protoclusters by (hub-)filamentary structures, the existence of massive starless cores, the physical and chemical properties of dense cores within protoclusters, and the feedback from already formed high-mass young protostars.

Key words: stars: formation — stars: kinematics and dynamics — ISM: clouds — ISM: molecules

1 INTRODUCTION

As the principal sources of heavy elements and UV radiation, high-mass stars ($M > 8 M_{\odot}$) play a major role in the evolution of galaxies. However, the formation mechanism of high-mass stars is still under intense debate (e.g., Zinnecker & Yorke 2007; Pineda et al. 2023). A variety of models have been proposed, contending with each other or focusing on different aspects of high-mass star formation. Early models disagreed about how a massive protostar obtains its initial mass and subsequently accretes additional mass. The competitive accretion scenario (e.g., Bonnell et al. 2004; Bonnell & Bate 2006) assumed initial fragmentation of a molecular cloud into low-mass cores each with mass approximately equal to the thermal Jeans mass. In contrast, the “turbulent core accretion model” (e.g., McKee & Tan 2003) suggested that high-mass stars form directly from turbulent massive gas cores. These idealized models depict protostars forming and accreting from their natal gas reservoirs which are treated as unstructured and obeying isotropic dynamics. Therefore, models that explained the presence of star forming regions in/on hierarchical structures, or more specifically filamentary structures, were put forward (e.g., global hierarchical collapse model, inertial-inflow model; Heitsch et al. 2008; Vázquez-Semadeni et al. 2009; Padoan et al. 2020). These models were partly supported by the observations of far-infrared dust continuum by the *Herschel* space observatory and other ground-based single-dishes, which demonstrated that filaments are ubiquitous and closely correlated with star formation in nearby molecular clouds as well as massive clumps in the Galactic Plane (e.g., André et al. 2010; Könyves et al. 2015; Li et al. 2016; Liu et al. 2018; Kumar et al. 2020; Schisano et al. 2020; Liu et al. 2021b; Hacar et al. 2023; Ge et al. 2023).

Observations show that high-mass stars are rare, and mostly born in massive clumps within the Galactic plane that are much denser than low-mass star forming clouds (e.g., Schuller et al. 2009). Considering their large distances (\sim kpc) and high dust extinction, studies of those massive clumps need high resolution interferometric observations that can resolve their internal gas structures and kinematics. The Atacama Large Millimeter/submillimeter Array (ALMA) provides an opportunity to investigate the inner hierarchical structures of high-mass star forming regions in great detail. There is growing evidence of the existence of filaments within massive clumps giving rise to hub-filamentary structures (HFSs) (e.g., Peretto et al. 2013; Yuan et al. 2018; Kumar et al. 2022; Liu et al. 2023a; Yang et al. 2023; Morii et al. 2023). However, most of these have been the results of case studies. The ‘ALMA Three-millimeter Observations of Massive Star-forming regions’ (ATOMS) survey (Liu et al. 2020a) observed 146 active

star-forming regions with ALMA at Band 3 ($\lambda \sim 3$ mm), aiming to systematically investigate the gas distribution, stellar feedback, and filaments inside massive clumps. The ATOMS survey revealed, in a statistical way, that HFSs are common within massive clumps (Zhou et al. 2022). Case studies of HFSs based on the ATOMS survey (Liu et al. 2022b,a; Xu et al. 2023a) confirmed that HFSs at scales from 0.1 pc to several pc play a key role in high-mass star formation, and the stellar feedback would in turn regulate the shapes and evolution of HFSs (e.g., Peretto et al. 2013; Kumar et al. 2022; Liu et al. 2023a). A higher-resolution (\sim 1000 au) survey would enable to systematically establish whether the hierarchical structures remain common down to a protocluster scale, and to provide for theoretical studies the observational constraints onto the detailed process of gas mass transport down to the protocluster scale.

Inspired by the ATOMS survey, we initiated the ‘Querying Underlying mechanisms of massive star formation with ALMA-Resolved gas Kinematics and Structures (QUARKS)’ survey programme at ALMA (PIs: Lei Zhu, Guido Garay and Tie Liu). The QUARKS survey selected the densest kernels of the massive clumps in the ATOMS survey, forming an unbiased sample (139) of protoclusters, and observed them at Band 6 ($\lambda \sim 1.3$ mm) of ALMA with much improved angular resolution than the ATOMS survey. The QUARKS survey aims (1) to statistically investigate the star formation process (e.g., fragmentation, outflows, disks) within an unbiased sample of protoclusters, (2) more specifically, to explore how (hub-)filamentary structures feed individual protostars within protoclusters, (3) to investigate the physical and chemical evolution of dense cores, and (4) to study various feedback mechanisms within protoclusters.

In this paper, we present an overall description of the QUARKS survey. The paper is structured as follows: In Section 2, we introduce the source sample and ALMA observations of the QUARKS survey. In Section 3, we describe the data reduction processes of both the continuum maps and spectral cubes. In Section 4, a first look at Sgr B2(M), a source within the sample of this survey, is presented to check the data quality and to explore in a preliminary fashion how the data can be linked to some of the science objectives of the QUARKS survey. In Section 5, we compare the QUARKS surveys with other ALMA programs and present more science topics that can be addressed by the QUARKS survey. A summary is provided in Section 7.

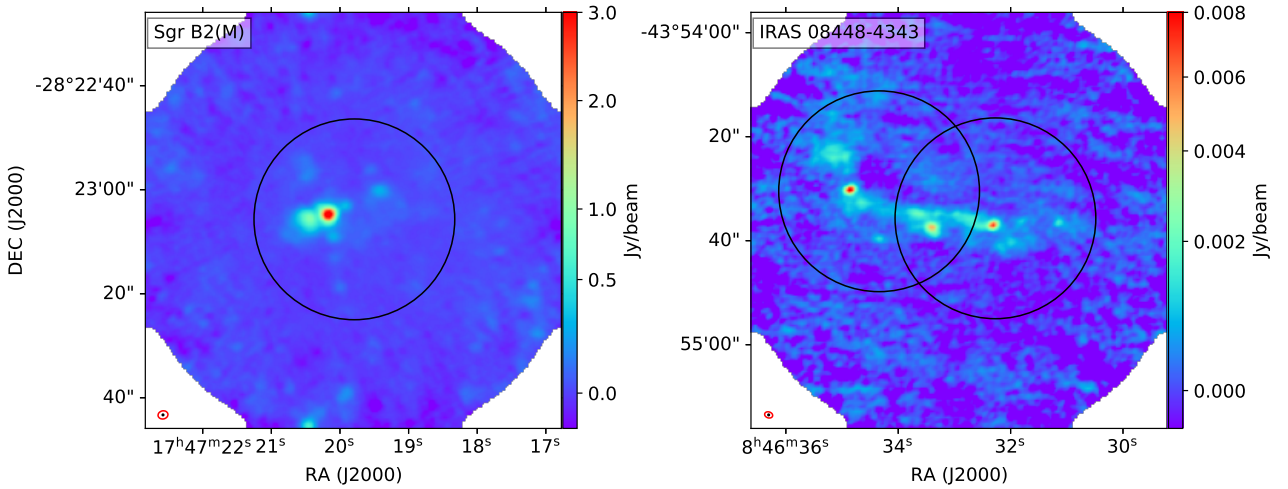


Fig. 1 Example of the targets of the QUARKS survey. In each panel, the background is the Band 3 continuum of the ATOMS survey. The black circle is primary beam of the ALMA 12-m array in Band 6. The red ellipse and the black dot in the lower-left corner show the angular resolutions of the ATOMS and QUARKS surveys, respectively.

2 SAMPLE AND OBSERVATIONS

2.1 Sample

The QUARKS sample contains 139 protoclusters, selected as the densest kernels of high-mass star forming regions revealed by the ATOMS survey (Liu et al. 2020a). Among the 146 sources of the ATOMS, two sources are low-mass clumps ($< 15 M_{\odot}$), four sources are dominated by extended HII regions with angular sizes larger than the primary beam at Band 6, and one source has no detection of continuum emission by ATOMS. The seven sources show no massive and compact kernels under the view of ATOMS and were thus excluded in the QUARKS sample. The ATOMS sources were selected as the bright sources ($T_b > 2$ K) of the CS $J = 2 - 1$ survey of Bronfman et al. (1996), a complete and homogeneous molecular line survey of UC HII region candidates in the Galactic plane. The ATOMS sample was also observed in the SIMBA survey, a 1.2 mm continuum emission survey using the SEST telescope by Faúndez et al. (2004), and the survey of HCN (4-3) and CS (7-6) using the ASTE telescope by Liu et al. (2016). The ALMA primary beam size at Band 6 is about 0.4 times the value in Band 3, hence the field of view (FoV) of the QUARKS survey can only cover part of the FoV of the ATOMS survey (Figure 1). For 17 sources with elongated and filamentary structures revealed by the 3 mm continuum emission of the ATOMS survey, two pointings for each were requested to entirely cover their dense kernels (e.g., IRAS 08448-4343 as shown in the right panel of Figure 1). In total, QUARKS has 156 single-pointings to observe 139 protoclusters. The clump masses (M_{clump}), quoted from Liu et al. (2020a), range from 40 to 2.5×10^5

M_{\odot} . These sources are located on the Galactic plane within a range of $|b| < 2.1^{\circ}$ and $-98.4^{\circ} < l < 43.8^{\circ}$, providing an unbiased sample of protoclusters in the inner Galactic plane. For all the targets of the QUARKS survey, the target names and target centers (in both Equatorial and Galactic coordinate systems) are listed in Table A.1.

Table 1 ALMA configurations of the QUARKS survey.

Configuration ⁽¹⁾	Resolution (arcsec)	MRS (arcsec)	rms _{line} ⁽²⁾ (mJy beam ⁻¹)
ACA	4.5	27	40
12-m array C-2	1	9	6
12-m array C-5	0.25	3.5	4
combined	0.3	27	3

⁽¹⁾ For a small fraction of the sources, the moderate-resolution observations were conducted by the C-3 (instead of the C-2) configuration, and the high-resolution observations were conducted by the C-6 (instead of the C-5) configuration.

⁽²⁾ The precise values of the line sensitivities (rms_{line}) of different sources vary by ~ 50 percent because of factors such as the integration time and calibration.

2.2 Re-evaluation of sample distance

The distances of the QUARKS sample (D^{old}) adopted by the ATOMS survey were initially derived from the velocities of CS $J = 2 - 1$ with an old Galactic rotation curve model (Bronfman et al. 1996). We updated the distances (D^{new}) using the distance calculator of Reid et al. (2016), based on the new systemic velocities of H^{13}CO^+ ($V_{\text{LSR}}^{\text{new}}$) measured from the ATOMS survey (Liu et al. 2020b). The distance calculator constrains the probability density function (PDF) of distance based on four types of information: kinematic distance (KD), the spiral arm model (SA),

Table 2 Set up of the spectral windows and the main targeted lines in the QUARKS survey.

SPW	f_{center} (GHz)	Bandwidth ⁽¹⁾ (GHz)	δV km s ⁻¹	Species	Trans. ⁽²⁾	E_u (K)	Note
SPW1	217.918429	1.875	1.344	SiO	5-4	31.2	Jet/shock/outflow tracer
				H ₂ CO	3-2	20–68	Temperature/infall/outflow tracer
				HC ₃ N	24-23	131	Infall/dense-gas/filament tracer
				CH ₃ OH	4 ₂ -3 ₁	45.5	Tracer of temperature/COMs
SPW2	220.318632	1.875	1.329	¹³ CO/C ¹⁸ O	2-1	16	Filament/outflow tracer
				CH ₃ CN	12-11	>68	Hot-core/massive-disk tracer
				SO	6-5	35	High-density/shock/outflow tracer
SPW3	231.369566	1.875	1.266	CO	2-1	16.6	Ambient-gas/outflow tracer
				N ₂ D ⁺	3-2	22.2	Cold-gas tracer
				¹³ CS	5-4	33.3	Ambient gas/filament tracer
				H ⁺ ⁽³⁾	H ₃₀ α		Ionized-gas/HII-region tracer
SPW4	233.519748	1.875	1.254	NH ₂ CHO	11-10	>94	Hot-core tracer
				C ₂ H ₅ CN	26-25	>100	Hot-core tracer
				SO ₂	– ⁽⁵⁾	>200	Tracer of sulfur-rich hot gas
				Continuum ⁽⁴⁾			Dust tracer

⁽¹⁾ The bandwidths listed here are for the 12-m-array observation. The bandwidth of each SPW of the ACA observations is 2 GHz.

⁽²⁾ The transitions of C₂H₅CN, NH₂CHO, and CH₃CN referred to line groups. The H₂CO has more than one transitions in SPW1. For these species, the ranges of E_u are listed.

⁽³⁾ H_{*n*}α is the transition of H atom but traces H⁺ (e.g., [Gordon & Sorochenko 2002](#); [Liu et al. 2023b](#)).

⁽⁴⁾ The SPW4 lacks low-energy lines and thus is good for extrating continuum emission (Section 3.2) and tracing hot cores (see Section 4.2).

⁽⁵⁾ Transitions of SO₂ such as 16_{6,10} – 17_{5,13} and 28_{3,25} – 28_{2,26} are covered by the SPW4.

Galactic latitude (GL), and parallax source (PS) with different weights, which were assumed to be 0.85, 0.15, 0.85, 0.15, respectively ([Reid et al. 2016](#)). The velocities and distances of the sample are listed in Table A.1.

As shown in Figure 2, the $V_{\text{LSR}}^{\text{old}}$ and $V_{\text{LSR}}^{\text{new}}$ are consistent with each other, and the standard deviation of their differences is ~ 1 km s⁻¹, much smaller than the virial velocity (σ_{vir}) of ~ 5 km s⁻¹ of giant molecular clouds ([Chevance et al. 2023](#)). Thus, the new calculated distance should not be influenced much by the new velocity employed. Moreover, we compared D^{new} and D^{old} , and found that they are consistent with each other with an 1- σ deviation of 0.7 kpc (Figure 2). The distribution of the QUARKS survey linear resolutions (estimated adopting an angular resolution of 0.3''; see Section 2.3) is shown as the green line in the lower panel of Figure 2. The distances (D^{new}) of the sample of the QUARKS survey range from 1.2 to 12.9 kpc. The median value of distances is 3.7 kpc, at which a linear resolution of 1100 au can be achieved. The resolutions for most sources are within the range of 500–2000 au (Figure 2).

2.3 ALMA Observations

We conducted single-pointing observations for the 156 targets of the QUARKS survey using the ALMA. The observations started from late October 2021 (Project IDs: 2021.1.00095.S, 2022.1.00298.S and 2023.1.00425.S; PI: Lei Zhu) with both the Atacama Compact 7-m Array (ACA) and the 12-m array of the ALMA at Band 6.

Observations with the ACA were completed in late May 2022. Observations with the 12-m Array have been partly executed in Cycles 8 and 9 and are expected to be completed in ALMA Cycle 10 (from October 2023 to September 2024).

For each source, observations in three different ALMA configurations were proposed. The observations in low, moderate and high resolution configurations were conducted by the ACA, ALMA 12-m array C-2 and C-5 configurations, respectively. In the ACA, C-2 and C-5 observations, the on-source time for one science target was approximately 5, 1, and 5 minutes, respectively. The typical values of the angular resolution, maximum recovering scale (MRS), and the sensitivity of spectral lines (rms_{line}) for different configurations, including the combined configuration, are summarized in Table 1. The continuum sensitivity (rms_{cont}) is not listed, because the rms_{cont} of the combined data varies in a wide range from 0.1 to several mJy beam⁻¹ for different sources, mostly because of the phase calibration and dynamic range limitations. Self-calibration was conducted for sources containing strong continuum (with peak value $\gtrsim 50$ mJy beam⁻¹) cores (Section 3). We note that for 1.3 mm continuum 1 mJy beam⁻¹ corresponds to a gas mass of 0.3 M_{\odot} at a distance of 5 kpc, derived assuming a median dust temperature of 30 K, a dust opacity per unit dust mass of 1 cm² g⁻¹ at 1.3 mm ([Ossenkopf & Henning 1994](#)), and a gas-to-dust mass ratio of 100. The angular resolutions of the combined images are typically better than 0.35 arcsec, which is about one-sixth of the resolution of the ATOMS sur-

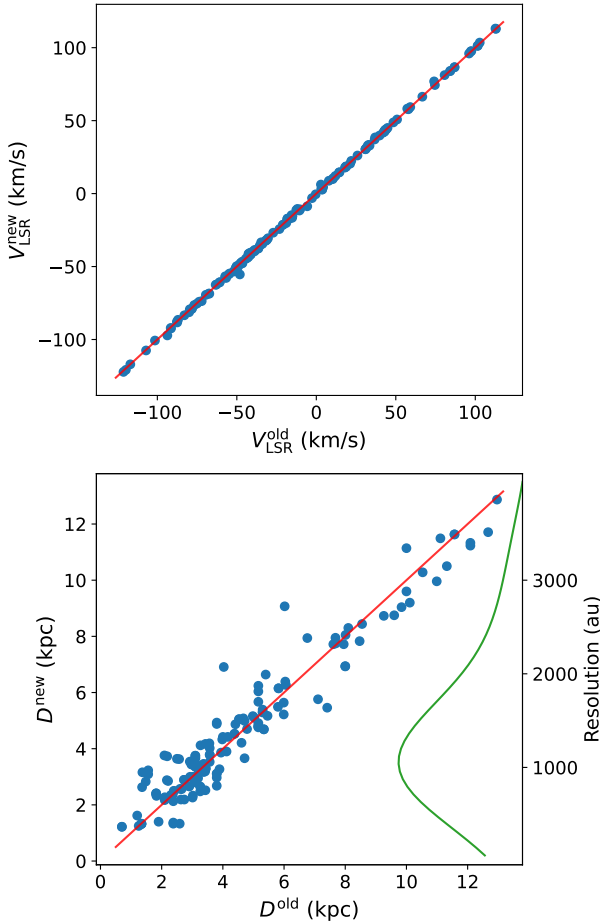


Fig. 2 Comparison between $V_{\text{LSR}}^{\text{new}}$ and $V_{\text{LSR}}^{\text{old}}$ is shown in the upper panel and between D^{new} and D^{old} (Lower) in the lower panel. The red lines represent $y = x$. The green curve represents the kernel distribution estimation of the source distances (with respect to the left Y axis) or of the Band-6 spatial resolution (with respect to the right Y axis) of the QUARKS sample.

vey (typically better than 2 arcsec) in Band 3 (Liu et al. 2020a). The significantly improved angular resolution of the QUARKS survey enables us to resolve dense cores, including massive starless core candidates and protostellar ones (star-forming dense cores, hot molecular cores and UC HII regions) within protoclusters, down to a physical scale of 3500 au in the most distant sources at a distance of ~ 10 kpc. For sources at a distance smaller than 3 kpc, the QUARKS survey can achieve a linear resolution better than 1000 au, and thus enable us to search for massive disk candidates (e.g., Johnston et al. 2015; Chen et al. 2016; Olguin et al. 2022).

The observations employed the Band 6 receivers in dual-polarization mode. Four spectral windows (SPW 1–4) were configured, and the frequency setups are shown in Table 2. The second, third and fourth columns of Table 2

list the central frequency, bandwidth and velocity resolution (δV) of each SPW (column 1). For the observations of the 12-m array and the ACA, each of the four SPWs has a bandwidth of 1.875 GHz and 2 GHz, respectively. The 5th to 7th columns of Table 2 list the parameters of the main transitions covered by each SPW, including the species name, transition labels, and upper-level energy (E_u). The four SPWs were configured to cover some commonly used lines including tracers for ambient gas (e.g., CO, ^{13}CO , C^{18}O), cold gas (N_2D^+), filament and infall (e.g., HC_3N), hot core (e.g., CH_3OH , $\text{C}_2\text{H}_5\text{CN}$, NH_2CHO), ionized gas ($\text{H}_{30}\alpha$), shocked gas (e.g., SiO, SO, H_2CO), and massive protostellar disk (CH_3CN), as listed in Table 2. SPW4 does not cover any low-energy strong lines (with upper-level energies $E_u < 100$ K) and thus is good for measuring the continuum emission. The Band 6 continuum is mainly produced by the dust emission. However, the Band-3 continuum emission of the ATOMS survey arises from a blend of thermal dust emission and free-free emission from ionized gas (Zhang et al. 2023a). Combining the data of the QUARKS and ATOMS surveys, the dust emission and the free-free emission can be partly decoupled.

The channel widths of the four SPWs are 976.563 kHz, corresponding to a δV of 1.25–1.35 km s^{-1} , depending on the rest frequency. The spectral resolution is better than that of the two wide-band SPWs (SPWs 7 and 8) of the ATOMS survey, ~ 1.6 km s^{-1} (Liu et al. 2020a). The velocity resolution of the QUARKS survey is high enough to spectrally resolve the emission lines of the outflows and ionized gas whose line wings or line widths are typically larger than 10 km s^{-1} (Liu et al. 2021a, 2022c; Zhang et al. 2022), and the emission of complex organic molecules (COMs) from hot cores ($\Delta V \sim 5$ km s^{-1} ; Qin et al. 2022; Taniguchi et al. 2023). The velocity gradients along the longest branches of HFSSs were systematically revealed in the ATOMS survey to be 8.7 $\text{km s}^{-1} \text{pc}^{-1}$ on average (Zhou et al. 2022), corresponding to a velocity difference of ~ 5 km s^{-1} at the maximum recovering scale (0.6 pc at a distance of 5 kpc) of the QUARKS survey. Thus, spectral lines of species such as HC_3N can be used to trace the multi-scale structures and gas kinematics within the clumps (Liu et al. 2022a; Xu et al. 2023a). The massive starless core candidates found so far tend to show no emission lines or narrow lines (with linewidths < 1 km s^{-1}) of cold gas tracers at Band 6 (e.g., Cyganowski et al. 2014; Kong et al. 2017). The N_2D^+ data of the QUARKS survey do not have sufficient spectral resolution to fully resolve the internal gas kinematics of possible massive starless cores found by this survey, but can provide us the spatial distribution of cold gas. The line widths of the (sub-)Keplerian disks around massive stars are typically 5–10 km s^{-1} (Johnston et al. 2015; Chen et al. 2016; Sanna

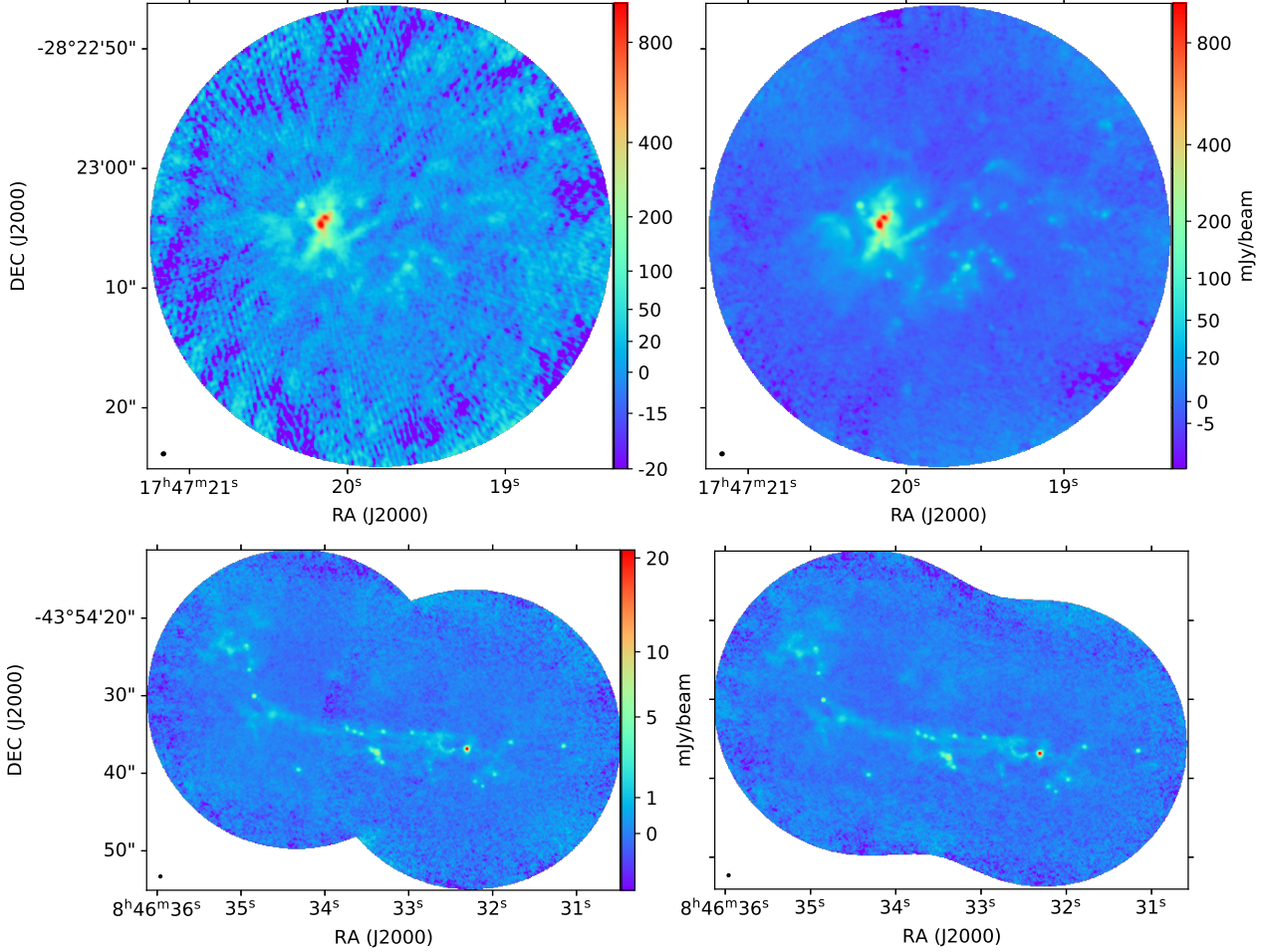


Fig. 3 The ALMA Band 6 continuum of Sgr B2(M) (upper) and IRAS 08448-4343 (lower). For Sgr B2(M), the upper right and upper left panels are the images with and without self-calibration, respectively. For IRAS 08448-4343, the lower left panel shows the image stitched from two independently cleaned images, and the lower right panel shows the the image cleaned from the combined visibility data. The two lower panels share the same colorbar. In each panel, primary beam correction has been applied, and the black small ellipse in the lower-left corner represents the synthesized beam.

et al. 2019). The velocity resolution of the QUARKS survey is high enough to spectrally resolve the massive disks, if detected. In a word, for most purposes, the spatial and spectral resolution in the QUARKS survey should be high enough for resolving the gas structures and kinematics in massive protoclusters.

3 DATA REDUCTION

The 12-m-array data and the ACA data of the QUARKS survey were combined to reveal both compact and extended emission. Sgr B2(M), also named I17441-2822 in this survey, is one of the QUARKS sources with most complex and richest line emission. It is very complicated to reduce the data and produce high-quality images for this object. In this work, we take Sgr B2(M) as an example for evaluating our data reduction procedure. The imaging was

carried out using the CASA software package of version 6.5 (McMullin et al. 2007).

3.1 Flagging of emission line channels

To separate the emission of continuum and spectral lines, the emission line channels need to be flagged. The spectral lines mainly contain the extended strong emission (e.g., the transitions with $E_u < 100$ K listed in Table 2) and the forest of COM lines from hot cores. Firstly, we identified all the transitions of strong lines within the four SPWs through matching the ALMA pipeline reduced datacubes and the laboratory databases for spectral lines (e.g., the CDMS; Müller et al. 2001). Since the V_{LSR} of the source is already known (Section 2.1), the observed frequencies of the those strong lines can be roughly determined. Because of the possible existence of multiple velocity components

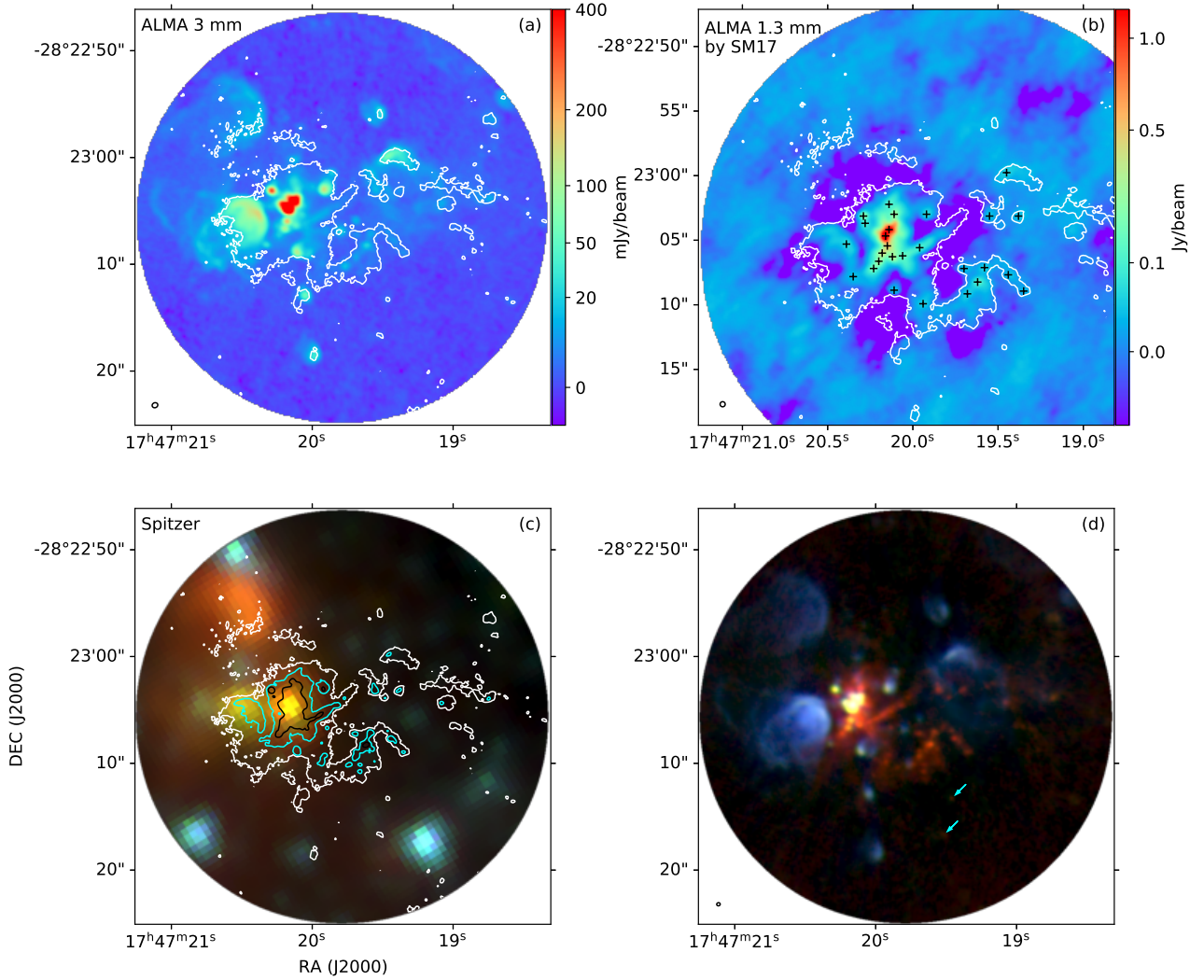


Fig. 4 (a) Image of the ALMA Band 3 continuum emission of Sgr B2(M) with a resolution of $\sim 0.5''$ by [Ginsburg et al. \(2018\)](#). The beam size is shown as an ellipse at the lower-left corner. The white contour shows the ALMA Band 6 (at 1.3 mm) continuum emission from the QUARKS survey at the level of 5σ ($2.5 \text{ mJy beam}^{-1}$). (b) Image of the ALMA Band 6 continuum emission from SM17 ([Sánchez-Monge et al. 2017](#)). The fields of view of SM17 and the QUARKS survey are not identical, but all 27 cores identified by [Sánchez-Monge et al. \(2017\)](#) marked by the black crosses are shown in this panel. Contour is the same as in panel (a). Note that the color map (*rainbow* with a power-law normalization with a power index of 0.4) is similar to that of Figure 3, where the ALMA Band 6 continuum of the QUARKS survey is shown. (c) Three-color image composed by the Spitzer 8 (red), 4.5 (green), 3.4 (blue) μm continuum. The white, cyan and black contours show the ALMA Band 6 continuum of the QUARKS survey, at the levels 2.5 , 15 , and 50 mJy beam^{-1} , respectively. (d) Three-color image composed of the ALMA Band 6 continuum of the QUARKS survey in red, the ALMA Band 3 continuum by [Ginsburg et al. \(2018\)](#) in green, and the VLA Band C (at $\sim 6 \text{ GHz}$) continuum by [Meng et al. \(2022\)](#) in blue. The cyan arrows pinpoint Cores 55 and 96 (see Figure 5 and Section 3.2.2). The beam size of the QUARKS survey is shown as an ellipse at the lower-left corner.

and of foreground absorption, an aggressive strategy was adopted for strong lines by flagging out all the channels within $\pm 50 \text{ km s}^{-1}$ of them.

For the line forest in hot cores, we first checked the fits cube of the ALMA pipeline products of the C-5 data, and manually extracted the spectra of hot cores. We calcu-

lated the rms of the unflagged channels, and then channels with intensity greater than $5 \times \text{rms}$ were flagged in our reduction. This procedure is repeated till we can no longer flag any more channels. Since the influence of the line forest is limited to hot cores, a relatively conservative strategy was adopted by flagging out the channels of $\pm 10 \text{ km s}^{-1}$

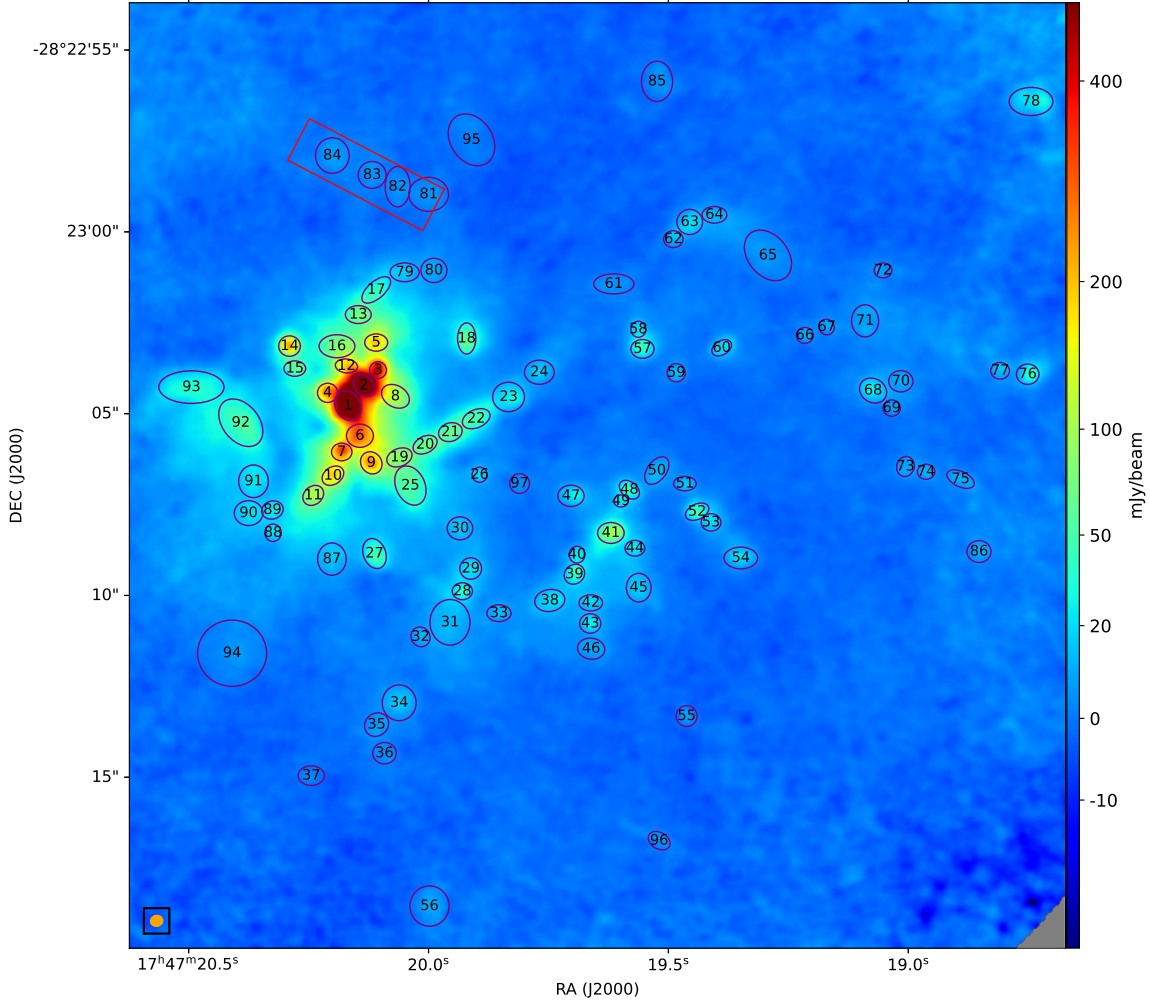


Fig. 5 Zoom in image of the right panel of Figure 3. The purple ellipses and black numbers marked the cores and substructures of Sgr B2(M) detected in the Band-6 continuum image (Section 4.1). The red rectangle marks the north arc of the Sgr B2(M). The orange ellipse in the lower-left corner represents the synthesized beam size.

around those lines. For a source with no fits cube produced by the ALMA pipeline, the channel flag of Sgr B2(M) was adopted as a template flag. We shifted the template flag before applying it to other sources according to their velocities (Table A.1). If the image quality of a source is not good because of an improper flag of emission line channels, we update the flag through checking the hot-core spectra extracted from its fits cube obtained in the first round of imaging and then conducted a second round of imaging.

3.2 Imaging and self-calibration of continuum data

To increase the sensitivity of the continuum image, data of all the four SPWs were used. The line-free channels (channels that have not been flagged out by the procedures described in Section 3.1) of both the ACA and 12-m-array data were fed to *CASA-tclean* to make the continuum maps. The Multi-scale Multi-Frequency Synthesis (*mtmfs*;

McMullin et al. 2007) with an *nterm* of 2 was chosen as the deconvolving algorithm. This algorithm is appropriate for cleaning on the combined visibility data of multiple configurations and multiple SPWs. The *briggs* weighting with a *robust* of 0.5 was adopted. For a source with strong continuum emission such as Sgr B2(M), self-calibration is necessary to improve the image quality (Section 3.2.1). For a source observed by two pointings such as the IRAS 08448-4343 (see Figure 3), we combined the visibility data of the two pointings before imaging.

3.2.1 Self-calibration of Sgr B2(M)

The 1.3 mm continuum of the Sgr B2(M) is very strong with a peak intensity (I_{peak}) of $\sim 1.2 \text{ Jy beam}^{-1}$ and a total flux of $> 23 \text{ Jy}$. A threshold of 20 mJy beam^{-1} was adopted for the first iteration of the cleaning process of the continuum image. A lower threshold resulted in diver-

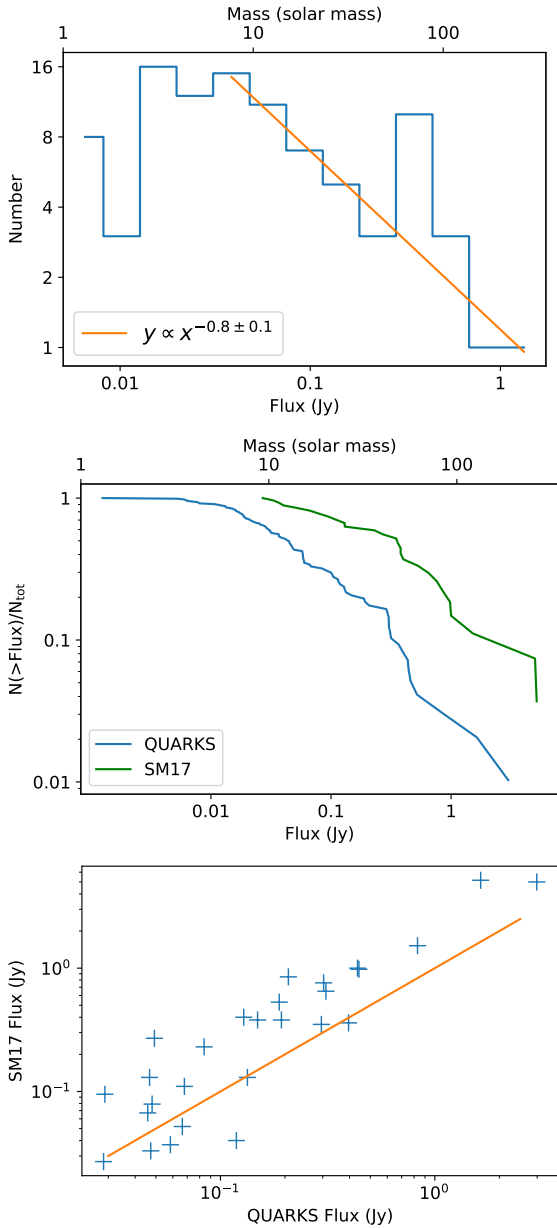


Fig. 6 Upper: The fluxes distribution of the cores in Sgr B2(M) (Figure 5). The orange line represents the power-law fitting of data at the high-flux end. Middle: The cumulative fluxes distribution of the cores in Sgr B2(M) by QUARKS (blue) and SM17 (green; Sánchez-Monge et al. 2017). For reference, the corresponding mass estimate as a first order of approximation (Section 4.1) is displayed at the top axis of the upper and middle panels. Lower: Comparison between the core fluxes measured by QUARKS and SM17. The orange line represents $y = x$. Note that QUARKS detected more fragmented cores than SM17 because of better angular resolution and sensitivity (Section 4.1).

gence. With that threshold, the reduced 1.3 mm continuum image of Sgr B2(M) show apparent fuzzy artifacts (left panel of Figure 3). This result agrees with a low dynamic range ($I_{\text{peak}}/rms_{\text{cont}} \sim 180$) for sources having complicated and strong continuum emission, implying that the systematic errors of the calibrations of phase and amplitudes dominate over the thermal noise. Self-calibration is a technique for correcting the visibility phases and/or amplitudes of a source by comparing the visibility data with a model of the source itself (e.g., Richards et al. 2022). For strong continuum sources like Sgr B2(M), self-calibration must be applied to improve its dynamic range.

The phases of the visibility data were self-calibrated based on the model of the first round of cleaning, following the CASA manual¹. A *solint* of 20 s was adopted for the *gaincal* task. Adopting a lower threshold (5 mJy beam⁻¹ for Sgr B2(M)), the continuum image was cleaned in the second round, and the model was updated accordingly. Then, both the phases and amplitudes of the visibility data were self-calibrated based on the updated model. Finally, adopting an even lower threshold (1.5 mJy beam⁻¹ for Sgr B2(M)), the cleaning process was conducted again to obtain the final continuum image. A rms of the residual map of 0.5 mJy was achieved through self-calibration for Sgr B2(M), corresponding to a dynamic range of greater than 2000. The final self-calibrated image greatly improves the quality compared with the non self-calibrated image. Extended structures that can only be marginally seen in previous observations (Figure 4) can be clearly recognized in the self-calibrated continuum image of the QUARKS survey, e.g, the north arc of Sgr B2(M) marked by the red rectangle in Figure 5 (see Section 3.2.2 for the discussion about the reliability of this structure). Approximately hundred cores or compact substructures can be identified in Sgr B2(M) from the Band 6 self-calibrated continuum image of this survey (see Figure 5 and Section 4.1 for details). Note that some of compact cores have weak continuum emission, which will be carefully scrutinized below for their reliability (see Section 3.2.2).

There is no general rule to choose the thresholds of self-calibration, and we conducted self-calibration manually and iteratively to optimize the thresholds that can avoid divergence while yielding good sensitivity. The continuum sensitivity of the QUARKS survey was expected to be 0.06 mJy beam⁻¹, according to the proposed observation design (Section 2.3). The final threshold of the continuum image of Sgr B2(M) is still higher than the expected sensitivity, mostly because (1) emission of Sgr B2(M) in Band 6 is dominated by strong spectral lines and thus the selection of line-free channels is difficult; (2)

¹ https://casaguides.nrao.edu/index.php?title=First_Look_at_Self_Calibration_CASA_6

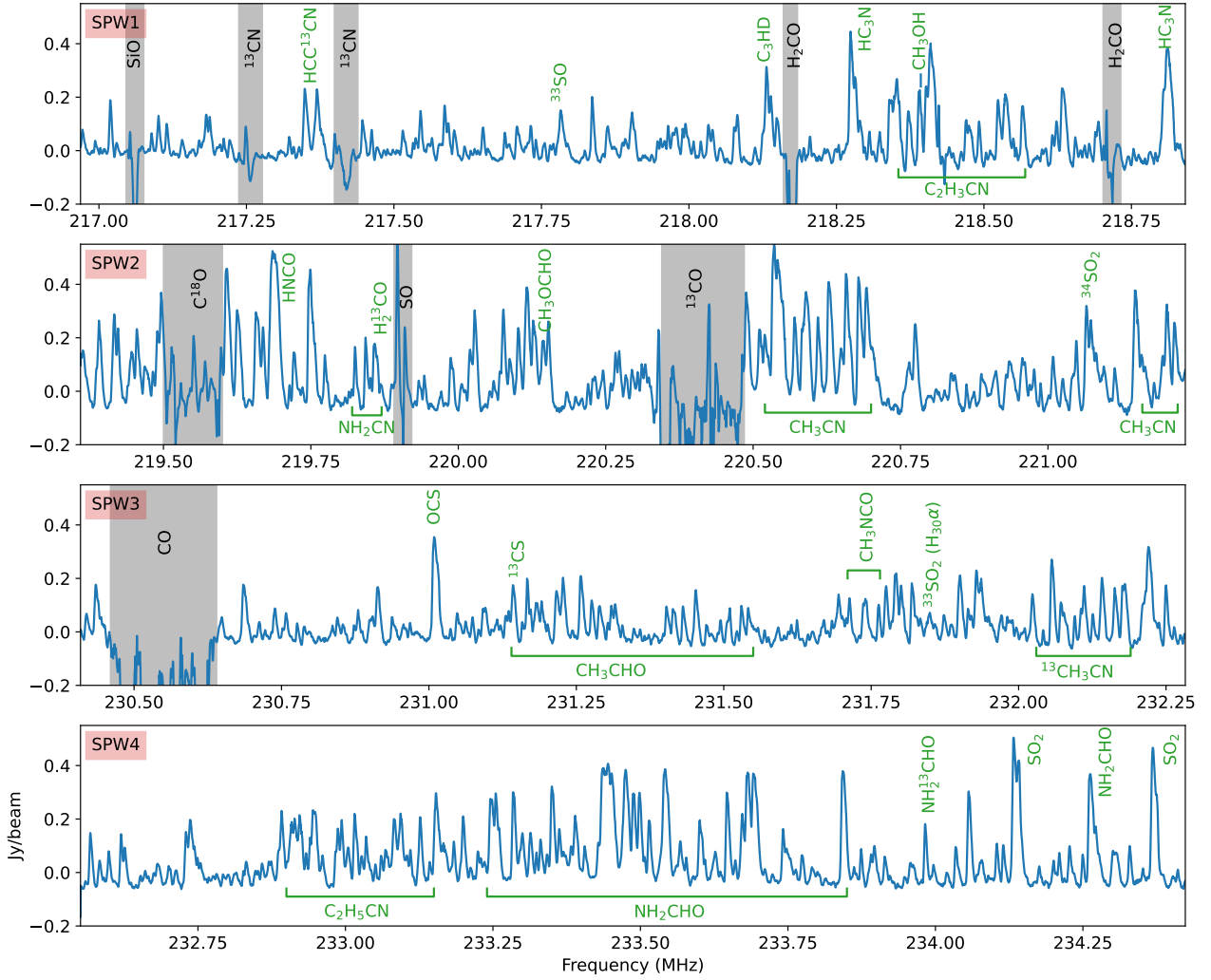


Fig. 7 The QUARKS spectra of core 6, the line-richest core among those in Figure 5. The gray shaded regions mark the strong lines showing absorption. The species of strong emission line or group of lines are labeled in green. Each of the labeled line groups is assigned to one species that dominates the spectral emission within the corresponding frequency range. The velocity (V_{LSR}) of core 6 is 67 km s^{-1} .

possible contamination comes from antenna sidelobes; (3) the strong and complex emission of Sgr B2(M) does not allow the self-calibration to further improve the dynamic range. Here we have conducted only two rounds of self-calibrations and additional rounds with more carefully chosen thresholds may further improve the image quality. For a weak source, such as I08448-4343, a final threshold of $0.2 \text{ mJy beam}^{-1}$ can be achieved without self-calibration, approaching the proposed 3σ sensitivity, and thus self-calibration is not required for it (lower panels of Figure 3).

3.2.2 Reliability of the self-calibration

To evaluate the reliability of our self-calibration, we examined the self-calibrated continuum image of Sgr B2(M)

from the QUARKS survey through comparing it with observations from different frequency bands (Figure 4). Sgr B2(M) was observed with ALMA at Band 6 by SM17 (Sánchez-Monge et al. 2017) in Cycle 2, with a resolution of $\sim 0.4''$, similar to the resolution of the QUARKS survey of $\sim 0.3''$. However, the sensitivity of SM17 is 8 mJy beam^{-1} , which is about 16 times lower than that of the QUARKS survey for Sgr B2(M) ($\sim 0.5 \text{ mJy beam}^{-1}$). The peak intensities of the Band 6 continuum of Sgr B2(M) are about 1.8 and 1.2 Jy beam^{-1} by SM17 and QUARKS, respectively, and are consistent with each other considering the different beam sizes and frequencies. All the cores of Sgr B2(M) identified by SM17 can be successfully recognized in the QUARKS continuum map (Section 4.1).

Two isolated cores, numbered 55 and 96 in Figure 5, are visible in the self-calibrated continuum map of the

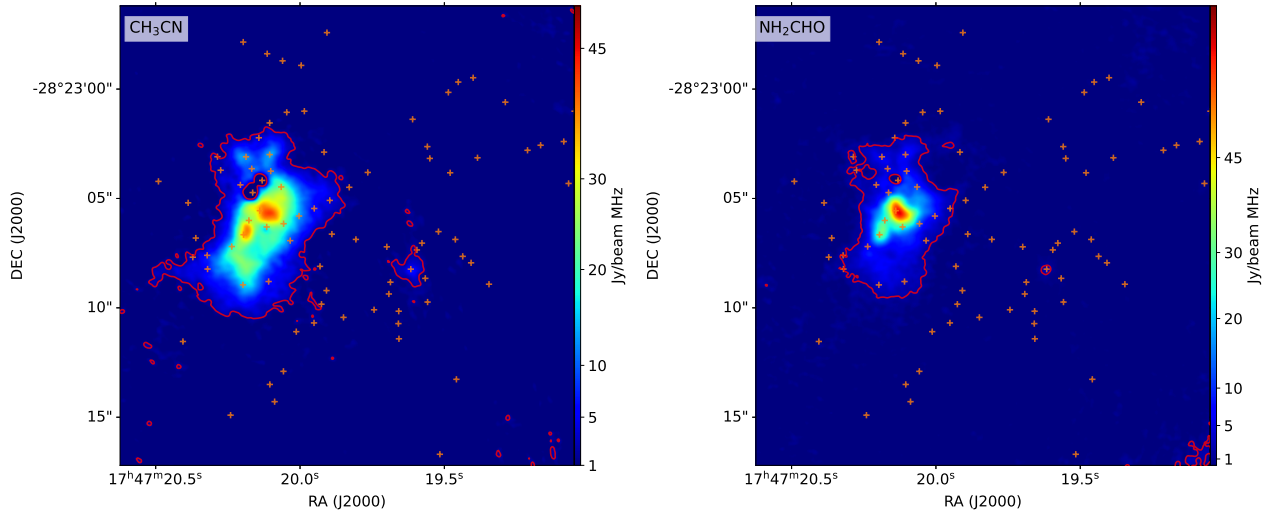


Fig. 8 Left: The intensity map integrated from 220.52 to 220.7 GHz, which contains a line group of CH_3CN as shown in Figure 7. Right: The intensity map integrated from 233.24 to 233.85 GHz, which contains a line group of NH_2CHO . In each panel, the red contour is for the intensity map with a level of $2 \text{ Jy beam}^{-1} \text{ MHz}$, and the orange crosses mark the continuum cores of this work.

QUARKS survey, but would be overwhelmed by noise if self-calibration were not applied (Figure 3). These cores are not visible in the continuum map of SM17 (see panel (b) of Figure 4), but are present in the ALMA Band 3 ($\lambda \sim 3 \text{ mm}$) continuum map observed by Ginsburg et al. (2018) with signal-to-noise ratios (S/Ns) greater than 5 at a resolution of $\sim 0.5''$ (see panel (a) of Figure 4). The long-baseline Band-6 observations by Budaiev et al. (2023) have also revealed these two cores at an angular resolution of $\sim 0.06''$. Thus, these two cores seen in the self-calibrated continuum map of the QUARKS survey should be reliable.

Core 97, with a weak peak intensity of 5 mJy beam^{-1} at Band 6 measured from the self-calibrated continuum image of the QUARKS survey, is located near the central crowded regions of Sgr B2(M). This core is not visible on the continuum map of SM17, but can be seen on the ALMA Band 3 (Ginsburg et al. 2018) and VLA Band C (6 GHz; Meng et al. 2022, see also panel (d) of Figure 4) continuum maps. Therefore, core 97 is considered reliable and could be an embedded UC HII region.

The north arc marked as a red rectangle in Figure 5 has not been reported previously. We checked the 3 mm continuum (Ginsburg et al. 2018) and the 1.3 mm continuum (Sánchez-Monge et al. 2017) from earlier observations and found tentative detection of the north arc (Figure 4), confirming its reliability. In conclusion, most, if not all, compact cores and extended structures in the continuum emission of the QUARKS survey can be reliably recovered by self-calibration in our data reduction.

3.3 Spectral cube

The calibration tables calculated from the self-calibration of continuum data were applied to all the channels, including the emission line channels. Subsequently, polynomial fitting was conducted to the data of the line-free channels in the visibility domain, and the continuum components were subtracted using the *uvcontsub* task of CASA. The visibility data of each SPW were then fed to *CASA-tclean* to generate cube of spectral lines. Thus, all the spectral cubes we generated are continuum-subtracted. The deconvolution algorithm of *tclean* was chosen as *multiscale*. Since the dynamic ranges of the spectral images are overall lower than that of continuum images, in practice, a uniform threshold of 15 mJy beam^{-1} (corresponding to a brightness temperature, T_b , threshold of 3.8 K for a beam size of $0.3''$) was chosen to optimize the performance of the cleaning of spectral cubes for most sources. As a result, the rms of the spectral cube of the QUARKS survey is $\sim 3 \text{ mJy beam}^{-1}$ per channel, equivalent to an rms of T_b of 0.8 K per channel.

4 A FIRST LOOK AT SGR B2(M)

The giant molecular cloud Sgr B2 is the most massive ($\sim 10^7 M_\odot$; e.g., Goldsmith et al. 1990) region with ongoing high-mass star formation in the Galaxy. It is an exceptional region in the Central Molecular Zone (CMZ), which appears to be deficient in star formation (e.g., Guesten & Downes 1983; Kauffmann et al. 2017). Its distance, estimated from the newest version of the distance calculator of Reid et al. (2016), is 8.3 kpc (Table A.1), consistent with

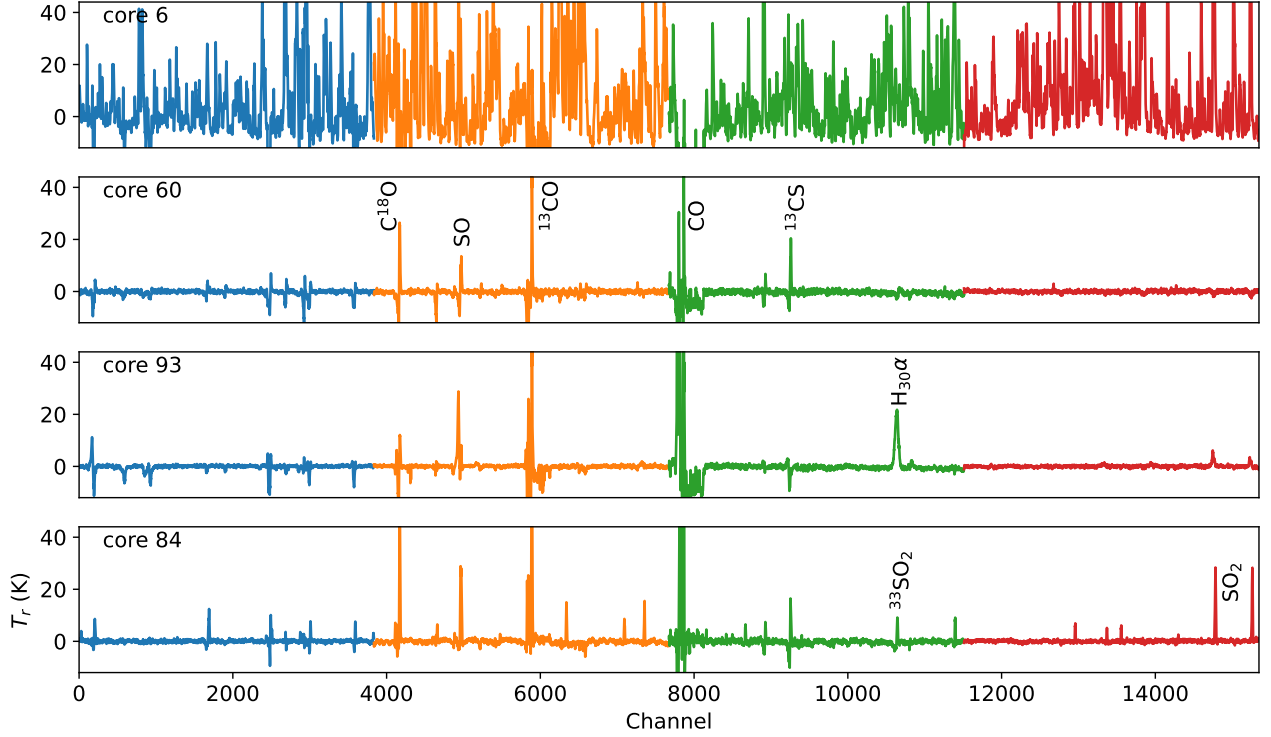


Fig. 9 Example spectra of cores of different types (Section 4.2). The blue, orange, green and red lines are the spectra of SPWs 1–4. See Figure 5 for the locations of these cores. The spectra of hot core (core 6) is for comparison. The core 84 shows more than 20 lines of sulfur-bearing species. See Figures 7 for the zoom-in spectra of core 6.

the values adopted by previous studies (e.g., Ginsburg et al. 2018; Meng et al. 2019) based on the results of Reid et al. (2014). Sgr B2(M) is one of the two most well-studied ‘hot cores’ (Sgr B2(M) and Sgr B2(N)) located in the central part of Sgr B2, which are actually high-mass protoclusters containing hundreds of protostellar cores (Ginsburg et al. 2018; Möller et al. 2023). Sgr B2 has also provided the detection of most molecules discovered so far in the interstellar medium, and thus is considered a very good target for studying astrochemistry (e.g., Belloche et al. 2008; McGuire 2022). In this section, we explore the continuum (Section 4.1) and spectral (Section 4.2) data, and present some links between the data and science topics of the QUARKS survey through a brief case study of Sgr B2(M).

4.1 Mini-starburst in the protocluster Sgr B2(M)

First, we manually identify the cores and core-like substructures in the continuum map using the image viewer CARTA². The criteria of a core are (1) it should have peak intensity larger than 5σ ; (2) it is isolated or the major part of its emission region should not merge into its neighbouring cores. In total, 97 cores were recognized. We then fitted these cores using 2-D Gaussian functions,

using the optimization algorithm provided by the Python package, *lmfit*³. The catalog of the cores, including the position, FWHMs of the major (L_{maj}) and minor (L_{min}) axes, position angle (PA), peak intensity (I_{peak}), and integrated flux are listed in Table A.2. The 1.3 mm observation of Sánchez-Monge et al. (2017) revealed 27 cores in Sgr B2(M), which are marked by the black crosses in panel (b) of Figure 4. We crosschecked the two core catalogs, and the results are listed in the last column of Table A.2. All the cores of Sánchez-Monge et al. (2017) can be identified in the QUARKS continuum image. The QUARKS survey has better angular resolution and continuum sensitivity compared with that of Sánchez-Monge et al. (2017), and thus our survey is capable of resolving many smaller-scale cores and identifying more weak entities. For example, the cluster of protostars located in the southwest of the central part of Sgr B2(M), which cannot be well resolved by Sánchez-Monge et al. (2017), is revealed in our survey as a collection of grape-like cores. These cores may have evolved from a hub-filamentary structure, but their intrinsic characteristics are to be further explored.

The fluxes of the cores identified in the QUARKS continuum image range from 5 mJy to 1 Jy. Assuming a uniform dust temperature of 100 K (the typical value of Sgr

² <https://cartavis.org/>

³ <https://pypi.org/project/lmfit/>

B2(M) by Möller et al. 2023) and a gas-to-dust mass ratio of 100, this corresponds to a mass range of approximately 1 to 100 M_{\odot} . For the brightest two cores (i.e., Cores 1 and 2 having $I_{\text{peak}} \gtrsim 0.5 \text{ Jy beam}^{-1}$), the optically-thin assumption could underestimate the core mass. For the remaining cores, their peak fluxes correspond to peak brightness temperatures lower than 100 K, suggesting that their mass estimate could not be severely affected by that assumption. The total mass of the cores in Sgr B2(M) is 2800 M_{\odot} , yielding a mean mass of 30 M_{\odot} , much lower than the value of Sánchez-Monge et al. (2017) which is 150 M_{\odot} . This is expected since the QUARKS survey can probe smaller fragmented scales of Sgr B2(M) due to higher sensitivity. The high-mass ($>5 M_{\odot}$) end of the core mass function (CMF) show a power-law distribution ($dN/d\log(m) \propto m^{-\alpha}$) with a power index of 0.8 ± 0.1 (Figure 6), implying a top-heavy shape as compared to the canonical initial mass function (Bastian et al. 2010; Sanhueza et al. 2019; Motte et al. 2022). The brightest cores may be even more massive if taking into account the effects of optical depths (Sánchez-Monge et al. 2017), which would result in a more top-heavy CMF. The kink in the high mass end result from the interference of dust shells of ionized regions (e.g., Cores 92 and 93 in Figure 5), which are extended and thus have relative large fluxes. The emission of the shells at 1.3 mm is probably highly contaminated by free-free ionized gas emission (Sánchez-Monge et al. 2017). The CMF of Sgr B2(M) is similar to that of Sgr B1-off, the mass range and power index of which are 0.3–230 M_{\odot} and 0.83 ± 0.21 , respectively (Lu et al. 2020). Note that Sgr B1-off is less evolved than Sgr B2(M), and a dust temperature of 20 K was adopted by Lu et al. (2020). These results may imply that the evolutionary tracks of the two regions may be regulated by some shared parameters of the environments, although the varying dust temperatures provide challenges for precisely deriving the core masses. On the other hand, the similarity of the CMFs between Sgr B2(M) and other high-mass star forming regions (with $\alpha < 1$; e.g., Cheng et al. 2018; Lu et al. 2020; Pouteau et al. 2023) implies that the QUARKS is sensitive enough to find out most of the high-mass cores in Sgr B2(M). The core density of Sgr B2(M) is then derived to be $\sim 100 \text{ pc}^{-2}$. This value is much higher than the value (19 pc^{-2}) of the mini-starburst ridges of W43 (Pouteau et al. 2022, 2023), implying stronger mini-starburst activities in Sgr B2(M) compared with the W43 mini-starburst region, an analog of a forming super star cluster (Bally et al. 2010).

4.2 COM-rich hot cores in Sgr B2(M)

Among the 97 cores, core 6 has the richest spectral line features (Figure 7). The spectra of core 6 are shown in Figure

7 as a gallery of the spectral lines that can be detected in the four SPWs of the QUARKS survey. Note that the spectra of core 6 do not contain all transitions that can be detected by the QUARKS survey. Some important lines listed in Table 2 can not be seen in the spectra of core 6. For example, no broad ($\Delta V > 20 \text{ km s}^{-1}$) line feature contributed by $\text{H}_{30}\alpha$ was detected. A weak and narrow ($\Delta V \sim 6 \text{ km s}^{-1}$) line feature can be seen at a frequency close to that of $\text{H}_{30}\alpha$, and this line feature can be assigned to a transition of $^{33}\text{SO}_2$ through LTE fitting as described in Liu et al. (2022d). It implies that the core 6 is a ‘pure’ hot core and does not harbor an UC HII region that is detectable by the QUARKS survey based on the data of $\text{H}_{30}\alpha$. The emission of N_2D^+ , a cold gas tracer, is also not detected in core 6, a COM-rich hot core.

We integrated the line groups of CH_3CN from 220.52 to 220.7 GHz and NH_2CHO from 233.24 to 233.85 GHz (see Figure 7), and the integrated intensity maps of the two line groups of Sgr B2(M) are shown in Figure 8. CH_3CN and NH_2CHO are both COM species, and the two line groups trace COM-rich hot gas. The emission of the two line groups is concentrated on a similar region, the central part of Sgr B2(M) with a size of $\sim 8''$ (0.3 pc). Therefore, the central part of Sgr B2(M) can be treated as a single ‘big hot core’. The molecular gas inside and among individual dense cores within this ‘big hot core’ is all COM-rich hot gas. The line group of NH_2CHO is more centrally peaked than that of CH_3CN , implying different excitation states or chemical segregation within the ‘big hot core’. The integrated intensity of the two line groups show another peak around core 41, which is more like a normal hot core heated by the massive protostars within it.

More than half of the continuum cores are not located within the COM-rich emission regions (Figure 8). Those cores can be divided into three types according to their spectral features, including (1) line-poor cores with no emission lines other than the strong lines of common species such as CO and ^{13}CS , (2) cores associated with HII regions showing strong emission of $\text{H}_{30}\alpha$, and (3) sulfur-rich cores with very strong emission of sulfur-bearing species such as SO, SO_2 , and their isotopologues.

We show the spectra of cores 60, 93, and 84 in Figure 9 as examples of types 1, 2, and 3, respectively. Core 60 of this work is one of the 27 cores identified by Sánchez-Monge et al. (2017) in Sgr B2(M). Sánchez-Monge et al. (2017) treated all those 27 cores as hot cores. However, some of these cores, such as their core A23 (core 60 in this work), exhibit a deficiency in spectral lines. The dust temperatures of these 27 cores of Sánchez-Monge et al. (2017) span a range of 46–162 K, as reported by Möller et al. (2023), with core A23 having a dust temperature of 72 ± 38 . Considering the diversity of dust temperatures, we classify

cores with COM-rich line features as hot cores, specifically those enclosed within the red contours in Figure 8. The sulfur-rich cores also tend to have high temperatures but are mainly located on the faint north arc (Figure 5), with a very different spatial distribution compared with other gas components of Sgr B2(M) (Liu et al. in prep).

5 SCIENTIFIC OBJECTIVES OF THE QUARKS SURVEY

Some scientific objectives (such as fragmentation, core mass function, astro-chemistry) of the QUARKS survey have been briefly mentioned above (Section 4), through looking at an exemplar source, the Sgr B2(M). There are, however, more science topics that can be addressed by the QUARKS survey data but have not been fully discussed, as discussed below.

Hunting for massive starless cores is an important topic of this project. Whether or not massive starless cores exist serves as a key discriminator between star formation theories, but still in dispute (e.g., McKee & Tan 2003; Bonnell et al. 2004; Heitsch et al. 2008). However, hunting for high-mass starless cores has proven to be very challenging, and only a few promising candidates have been reported (e.g., Cyganowski et al. 2014; Wang et al. 2014; Kong et al. 2017). Most of the efforts in the search for massive starless cores have been focused on the early stages of massive clumps (e.g., infrared dark clouds). However, observations indicated that gas accretion inside protoclusters (e.g., through hub-filamentary structures) would continue before being destroyed by stellar feedback (e.g., Sanhueza et al. 2021; Zhou et al. 2022; Xu et al. 2023b). Several numerical simulations suggest that thermal feedback from OB protostars and the strong magnetic field of proto-stellar clusters can play a crucial role in reducing the level of fragmentation and producing massive dense cores (e.g., Krumholz et al. 2007; Offner et al. 2009; Myers et al. 2013). Thus, it is possible that the newly assembled gas within evolving protoclusters could form massive starless cores. During the pioneer exploration of the QUARKS data, we have found a massive starless core candidate in I18507+0121, which shows no emission lines except for the line of N_2D^+ (Mai et al. in prep). The QUARKS survey can provide the high-mass star formation community additional samples of massive pre-stellar cores to explore.

How stellar feedback from outflows, HII regions and stellar winds from formed OB protostars influences the formation of new generation of stars and reshapes gas distribution in clouds is highly debated (e.g., Krumholz et al. 2014; Peters et al. 2017; Schneider et al. 2020; Zhang et al. 2023b; Pouteau et al. 2023; Herrington et al. 2023). The ATOMS survey studied the impact of UC HII regions (Zhang et al. in prep.) on their surrounding molecular gas,

but detailed investigation was limited by sensitivity, and resolution. The high resolution of the QUARKS survey could help to study how the feedback of UC HII regions (traced by $H_{30\alpha}$) influence the surrounding star formation activities, e.g., the core masses under the impact of HII region on a scale of thousands au. The thermal feedback (e.g. shocks) from the ionized gas of the young HII regions could be reflected in the velocity and temperature distributions over the surrounding dense cores, which could be revealed by molecular transitions such as CH_3CN , CH_3OH and their isotopologues (Moscadelli et al. 2018). The outflow tracers such as ^{12}CO J=2-1, ^{13}CO J=2-1 and SiO J=5-4 included in the QUARKS survey are very helpful for detecting molecular outflows and investigate the role of outflow feedback in maintain turbulence (e.g., Li et al. 2020; Baug et al. 2021) or heating gas (Wang et al. 2012) in gas clumps.

For protocluster within 3 kpc, a resolution of better than 1000 au would enable us to search for massive disks (Chen et al. 2016) and large-scale (>10,000 au) gas streamers or spiral arms that may feed the disks (Pineda et al. 2020; Lee et al. 2023) with various gas tracers (e.g., CH_3CN , SO).

Simulations and recent observational studies revealed time-dependent co-evolution between clump and core masses (e.g., Bonnell et al. 2004; Anderson et al. 2021; Sanhueza et al. 2019; Xu et al. 2023b). The QUARKS survey would help to reveal the co-evolution between protoclusters and protostars in different environments. Species such as N_2D^+ , H_2CO , CH_3CN , and SO_2 are good tracers of gas temperature ranging from 10's to hundreds Kelvin, enabling the QUARKS survey to investigate the evolution of cores in different stages and other substructures found inside protoclusters. We expect that the QUARKS survey can help the study of the co-evolution of the multi-scale structures of/within protoclusters, through case studies of typical sources, and, more importantly, through unbiased statistical studies.

6 LINK TO OTHER ALMA LARGE SURVEY PROGRAMS

High-resolution follow-up studies of the discoveries and investigations carried out in the ATOMS survey (Liu et al. 2020a) is an important goal of the QUARKS survey. How the protostars in protoclusters accumulate mass and in turn affect their natal clumps and regulate new star formation is an important topic for both projects. The ATOMS survey has revealed ubiquitous filaments as well as filament-hub systems (HFSs) in protoclusters from dense core scales (~ 0.1 pc) to clump/cloud scales (~ 1 -10 pc), and has found evidences for filamentary accretion at all scales (Zhou et al. 2022). The QUARKS survey can be used to check whether

HFSs will further fragment down to a scale of 0.01 pc, and can inspect how they feed individual protostars within protoclusters. The QUARKS survey could also be used to establish the sample of hot cores. The ATOMS survey found 60 hot cores, contributing so far the largest uniform sample of hot cores observed with similar angular resolution and spectral coverage (Qin et al. 2022). The QUARKS survey, with much higher resolution, will resolve these hot cores, and help to statistically study the chemical diversities of COMs and the evolution of hot cores.

Some large programs of ALMA, e.g., the ALMA-IMF (Motte et al. 2022) and ALMAGAL (PI: Sergio Molinari), have science goals similar to or overlapping with that of the QUARKS survey. Compared with those programs, the QUARKS survey has some unique advantages. The ALMA-IMF observed 15 extreme ($M_{\text{clump}} > 2500 M_{\odot}$) and nearby (2–5.5 kpc) protoclusters in mosaic mode at a spatial resolution of ~ 2000 au, aiming to make breakthroughs in studying the origin of the initial mass function (IMF) of stars. The single pointing mode of the QUARKS survey enables to generate quickly observe a relatively larger (139) and unbiased (Section 2.1) sample of protoclusters. Guided by the observations of the ATOMS survey in Band 3 (Liu et al. 2020a), QUARKS focuses on the dense kernels of the protoclusters that harbour majority of the massive protostars. In Sgr B2(M), only 5 compact cores were detected by the ATOMS survey, and the number by the QUARKS survey is more than 15 times that value. In the weak-continuum source, IRAS 08448-4343, more than 20 dense cores have been revealed by the QUARKS survey (Figure 3). The ATOMS survey identified 453 compact cores, and it is reasonable to expect that the QUARKS survey would detect at least 10 dense cores for each source on average and 1500 ones in total. The total bandwidth (7.5 GHz) of the QUARKS survey is twice the total bandwidth (3.75 GHz) of the ALMA-IMF. The wide bandwidth makes the QUARKS survey ideal for studying the chemical properties of individual protostars and of the protocluster as a whole, e.g., investigating the chemical differentiation between O- and N-bearing COMs (e.g., Wyrowski et al. 1999; Qin et al. 2022; Peng et al. 2022), and exploring the formation mechanisms for individual complex organic molecules (e.g., CH_3COCH_3 and CH_3CHO , Shi et al. 2023, submitted). The QUARKS survey can help to statistically study the properties of protostars in an unbiased sample of protoclusters, and thus fully investigate the CMF at the high-mass end in widely different Galactic environments and at different evolutionary stages, binned by distances and protocluster properties.

ALMAGAL observed more than 1000 dense clumps with $M > 500 M_{\odot}$ and $d < 7.5$ kpc with a linear resolution of ~ 1000 au and a mass sensitivity of $0.3 M_{\odot}$ at 1.3

mm, similar to the QUARKS survey. All the four SPWs of ALMAGAL are located within the frequency range of 216.9–221 GHz, corresponding to the SPWs 1 and 2 of the QUARKS survey. Emission lines of some important species, such as ^{12}CO and N_2D^+ , and strong recombination lines (the α lines of hydrogen) were not covered by ALMAGAL. QUARKS covered the transitions of all the three isotologues of carbon monoxide (CO , ^{13}CO and C^{18}O), and in combination with the ATOMS survey, we can study the large-scale kinematics and structures up to 1 pc ($30''$ at a distance of 8 kpc). N_2D^+ is very helpful for searching massive starless cores (Kong et al. 2017). Furthermore, the SPW4 of the QUARKS survey is free of strong lines, and it is very useful for searching and studying COMs in hot cores (Figure 7), while recombination lines could help identify HII regions.

7 SUMMARY

We have presented an overview of the ALMA-QUARKS survey. The survey is observing 139 protoclusters, consisting of 156 pointings with the ALMA at Band 6. These protoclusters were selected as the dense kernels of massive clumps revealed by the ATOMS survey. The primary goal of the QUARKS survey was to investigate the star formation process within protoclusters down to a scale of 1000 au in an unbiased and statistical manner. This paper has outlined the observations and data reduction of the QUARKS survey, and provides a first look at Sgr B2(M). The QUARKS survey's wide bandwidth (7.5 GHz) and high resolution ($\sim 0.3''$) allow us to resolve more compact cores than the ATOMS survey, and detect previously unrevealed fainter filamentary structures. The spectral windows cover transitions of species such as CO , SO , N_2D^+ , SiO , H_3O^+ , and many complex organic molecules, tracing gas components with varying temperatures and spatial extents. The unique observing setups of the QUARKS survey offer an opportunity to enhance our understanding of several scientific topics of star formation, including the mass transfer process inside protoclusters by hub-filamentary structures, the existence of massive starless cores, the physical and chemical properties of dense cores within protoclusters, and protocluster feedback. Preliminary analysis towards Sgr B2 (M2) indicates that our data reduction ensures high-quality continuum and spectral line data for realizing these scientific objectives. Specifically, the self-calibration approach can further improve data quality particularly for targeted sources with strong emission.

Acknowledgements This work has been supported by the National Key R&D Program of China (No. 2022YFA1603100), National Natural Science Foundation of China (NSFC) through grants No. 12203086, 12033005, 12073061, 12122307,

and 12103045. Moreover, X.L. has also been supported by CPSF No. 2022M723278; T.L. by the international partnership program of Chinese Academy of Sciences through grant No.114231KYSB20200009, Shanghai Pujiang Program 20PJ1415500, the science research grants from the China Manned Space Project with no. CMS-CSST-2021-B06; H.L. by Yunnan Fundamental Research Project (grant No.202301AT070118). This research was carried out in part at the Jet Propulsion Laboratory, which is operated by the California Institute of Technology under a contract with the National Aeronautics and Space Administration (80NM0018D0004). AS, GG, LB, and DM acknowledge support from the ANID BASAL project FB210003. AS also acknowledges support from the Fondecyt Regular (project code 1220610). PS was partially supported by a Grant-in-Aid for Scientific Research (KAKENHI Number JP22H01271 and JP23H01221) of JSPS. K.T. was supported by JSPS KAKENHI (Grant Number JP20H05645). This paper makes use of the following ALMA data: ADS/JAO.ALMA#2019.1.00685.S, 2021.1.00095.S and 2023.1.00425. ALMA is a partnership of ESO (representing its member states), NSF (USA) and NINS (Japan), together with NRC (Canada), MOST and ASIAA (Taiwan), and KASI (Republic of Korea), in cooperation with the Republic of Chile. The Joint ALMA Observatory is operated by ESO, AUI/NRAO and NAOJ. We show warm thanks to the anonymous referee for providing helpful comments for improving the paper.

References

- Anderson, M., Peretto, N., Ragan, S. E., et al. 2021, *MNRAS*, 508, 2964 [14](#)
- André, P., Men'shchikov, A., Bontemps, S., et al. 2010, *A&A*, 518, L102 [2](#)
- Bally, J., Anderson, L. D., Battersby, C., et al. 2010, *A&A*, 518, L90 [13](#)
- Bastian, N., Covey, K. R., & Meyer, M. R. 2010, *ARA&A*, 48, 339 [13](#)
- Baug, T., Wang, K., Liu, T., et al. 2021, *MNRAS*, 507, 4316 [14](#)
- Belloche, A., Menten, K. M., Comito, C., et al. 2008, *A&A*, 482, 179 [12](#)
- Bonnell, I. A., & Bate, M. R. 2006, *MNRAS*, 370, 488 [2](#)
- Bonnell, I. A., Vine, S. G., & Bate, M. R. 2004, *MNRAS*, 349, 735 [2, 14](#)
- Bronfman, L., Nyman, L. A., & May, J. 1996, *A&AS*, 115, 81 [3, 20](#)
- Budaiev, N., Ginsburg, A., Jeff, D., et al. 2023, Protostellar cores in Sagittarius B2 N and M, *arXiv:2309.14407* [11](#)
- Chen, H.-R. V., Keto, E., Zhang, Q., et al. 2016, *ApJ*, 823, 125 [5, 14](#)
- Cheng, Y., Tan, J. C., Liu, M., et al. 2018, *ApJ*, 853, 160 [13](#)
- Chevance, M., Krumholz, M. R., McLeod, A. F., et al. 2023, in *Astronomical Society of the Pacific Conference Series*, Vol. 534, Protostars and Planets VII, ed. S. Inutsuka, Y. Aikawa, T. Muto, K. Tomida, & M. Tamura, 1 [4](#)
- Cyganowski, C. J., Brogan, C. L., Hunter, T. R., et al. 2014, *ApJ*, 796, L2 [5, 14](#)
- Faúndez, S., Bronfman, L., Garay, G., et al. 2004, *A&A*, 426, 97 [3](#)
- Ge, Y., Wang, K., Duarte-Cabral, A., et al. 2023, *A&A*, 675, A119 [2](#)
- Ginsburg, A., Bally, J., Barnes, A., et al. 2018, *ApJ*, 853, 171 [7, 11, 12](#)
- Goldsmith, P. F., Lis, D. C., Hills, R., & Lasenby, J. 1990, *ApJ*, 350, 186 [11](#)
- Gordon, M. A., & Sorochenko, R. L. 2002, *Radio Recombination Lines. Their Physics and Astronomical Applications*, Vol. 282 (Berlin: Springer) [4](#)
- Guesten, R., & Downes, D. 1983, *A&A*, 117, 343 [11](#)
- Hacar, A., Clark, S. E., Heitsch, F., et al. 2023, in *Astronomical Society of the Pacific Conference Series*, Vol. 534, Protostars and Planets VII, ed. S. Inutsuka, Y. Aikawa, T. Muto, K. Tomida, & M. Tamura, 153 [2](#)
- Heitsch, F., Hartmann, L. W., Slyz, A. D., Devriendt, J. E. G., & Burkert, A. 2008, *ApJ*, 674, 316 [2, 14](#)
- Herrington, N. P., Dobbs, C. L., & Bending, T. J. R. 2023, *MNRAS*, 521, 5712 [14](#)
- Johnston, K. G., Robitaille, T. P., Beuther, H., et al. 2015, *ApJ*, 813, L19 [5](#)
- Kauffmann, J., Pillai, T., Zhang, Q., et al. 2017, *A&A*, 603, A89 [11](#)
- Kong, S., Tan, J. C., Caselli, P., et al. 2017, *ApJ*, 834, 193 [5, 14, 15](#)
- Könyves, V., André, P., Men'shchikov, A., et al. 2015, *A&A*, 584, A91 [2](#)
- Krumholz, M. R., Klein, R. I., & McKee, C. F. 2007, *ApJ*, 656, 959 [14](#)
- Krumholz, M. R., Bate, M. R., Arce, H. G., et al. 2014, in *Protostars and Planets VI*, ed. H. Beuther, R. S. Klessen, C. P. Dullemond, & T. Henning, 243 [14](#)
- Kumar, M. S. N., Arzoumanian, D., Men'shchikov, A., et al. 2022, *A&A*, 658, A114 [2](#)
- Kumar, M. S. N., Palmeirim, P., Arzoumanian, D., & Inutsuka, S. I. 2020, *A&A*, 642, A87 [2](#)
- Lee, J.-E., Matsumoto, T., Kim, H.-J., et al. 2023, *ApJ*, 953, 82 [14](#)
- Li, G.-X., Urquhart, J. S., Leurini, S., et al. 2016, *A&A*, 591, A5 [2](#)
- Li, S., Sanhueza, P., Zhang, Q., et al. 2020, *ApJ*, 903, 119 [14](#)
- Liu, H.-L., Liu, T., Evans, Neal J., I., et al. 2021a, *MNRAS*, 505, 2801 [5](#)

- Liu, H.-L., Tej, A., Liu, T., et al. 2022a, MNRAS, 511, 4480 [2](#), [5](#)
- Liu, H.-L., Tej, A., Liu, T., et al. 2022b, MNRAS, 510, 5009 [2](#)
- Liu, H.-L., Tej, A., Liu, T., et al. 2023a, MNRAS, 522, 3719 [2](#)
- Liu, R., Liu, T., Chen, G., et al. 2022c, MNRAS, 511, 3618 [5](#)
- Liu, T., Kim, K.-T., Yoo, H., et al. 2016, ApJ, 829, 59 [3](#)
- Liu, T., Kim, K.-T., Juvela, M., et al. 2018, ApJS, 234, 28 [2](#)
- Liu, T., Evans, N. J., Kim, K.-T., et al. 2020a, MNRAS, 496, 2790 [2](#), [3](#), [5](#), [14](#), [15](#)
- Liu, T., Evans, N. J., Kim, K.-T., et al. 2020b, MNRAS, 496, 2821 [3](#)
- Liu, X. C., Wu, Y., Zhang, C., et al. 2021b, ApJ, 912, 148 [2](#)
- Liu, X., Liu, T., Shen, Z., et al. 2022d, ApJS, 263, 13 [13](#)
- Liu, X., Liu, T., Shen, Z., et al. 2023b, A&A, 671, L1 [4](#)
- Lu, X., Cheng, Y., Ginsburg, A., et al. 2020, ApJ, 894, L14 [13](#)
- McGuire, B. A. 2022, ApJS, 259, 30 [12](#)
- McKee, C. F., & Tan, J. C. 2003, ApJ, 585, 850 [2](#), [14](#)
- McMullin, J. P., Waters, B., Schiebel, D., Young, W., & Golap, K. 2007, in Astronomical Society of the Pacific Conference Series, Vol. 376, Astronomical Data Analysis Software and Systems XVI, ed. R. A. Shaw, F. Hill, & D. J. Bell, 127 [6](#), [8](#)
- Meng, F., Sánchez-Monge, Á., Schilke, P., et al. 2019, A&A, 630, A73 [12](#)
- Meng, F., Sánchez-Monge, Á., Schilke, P., et al. 2022, A&A, 666, A31 [7](#), [11](#)
- Möller, T., Schilke, P., Sánchez-Monge, Á., Schmiedeke, A., & Meng, F. 2023, A&A, 676, A121 [12](#), [13](#)
- Morii, K., Sanhueza, P., Nakamura, F., et al. 2023, ApJ, 950, 148 [2](#)
- Moscadelli, L., Rivilla, V. M., Cesaroni, R., et al. 2018, A&A, 616, A66 [14](#)
- Motte, F., Bontemps, S., Csengeri, T., et al. 2022, A&A, 662, A8 [13](#), [15](#)
- Müller, H. S. P., Thorwirth, S., Roth, D. A., & Winnewisser, G. 2001, A&A, 370, L49 [6](#)
- Myers, A. T., McKee, C. F., Cunningham, A. J., Klein, R. I., & Krumholz, M. R. 2013, ApJ, 766, 97 [14](#)
- Offner, S. S. R., Hansen, C. E., & Krumholz, M. R. 2009, ApJ, 704, L124 [14](#)
- Olguin, F. A., Sanhueza, P., Ginsburg, A., et al. 2022, ApJ, 929, 68 [5](#)
- Ossenkopf, V., & Henning, T. 1994, A&A, 291, 943 [4](#)
- Padoan, P., Pan, L., Juvela, M., Haugbølle, T., & Nordlund, Å. 2020, ApJ, 900, 82 [2](#)
- Peng, Y., Liu, T., Qin, S.-L., et al. 2022, MNRAS, 512, 4419 [15](#)
- Peretto, N., Fuller, G. A., Duarte-Cabral, A., et al. 2013, A&A, 555, A112 [2](#)
- Peters, T., Naab, T., Walch, S., et al. 2017, MNRAS, 466, 3293 [14](#)
- Pineda, J. E., Segura-Cox, D., Caselli, P., et al. 2020, Nature Astronomy, 4, 1158 [14](#)
- Pineda, J. E., Arzoumanian, D., Andre, P., et al. 2023, in Astronomical Society of the Pacific Conference Series, Vol. 534, Protostars and Planets VII, ed. S. Inutsuka, Y. Aikawa, T. Muto, K. Tomida, & M. Tamura, 233 [2](#)
- Pouteau, Y., Motte, F., Nony, T., et al. 2022, A&A, 664, A26 [13](#)
- Pouteau, Y., Motte, F., Nony, T., et al. 2023, A&A, 674, A76 [13](#), [14](#)
- Qin, S.-L., Liu, T., Liu, X., et al. 2022, MNRAS, 511, 3463 [5](#), [15](#)
- Reid, M. J., Dame, T. M., Menten, K. M., & Brunthaler, A. 2016, ApJ, 823, 77 [3](#), [4](#), [11](#), [20](#)
- Reid, M. J., Menten, K. M., Brunthaler, A., et al. 2014, ApJ, 783, 130 [12](#)
- Richards, A. M. S., Moravec, E., Etoke, S., et al. 2022, arXiv e-prints, arXiv:2207.05591 [9](#)
- Sánchez-Monge, Á., Schilke, P., Schmiedeke, A., et al. 2017, A&A, 604, A6 [7](#), [9](#), [10](#), [11](#), [12](#), [13](#), [23](#)
- Sanhueza, P., Contreras, Y., Wu, B., et al. 2019, ApJ, 886, 102 [13](#), [14](#)
- Sanhueza, P., Girart, J. M., Padovani, M., et al. 2021, ApJ, 915, L10 [14](#)
- Sanna, A., Kölligan, A., Moscadelli, L., et al. 2019, A&A, 623, A77 [5](#)
- Schisano, E., Molinari, S., Elia, D., et al. 2020, MNRAS, 492, 5420 [2](#)
- Schneider, N., Simon, R., Guevara, C., et al. 2020, PASP, 132, 104301 [14](#)
- Schuller, F., Menten, K. M., Contreras, Y., et al. 2009, A&A, 504, 415 [2](#)
- Taniguchi, K., Sanhueza, P., Olguin, F. A., et al. 2023, ApJ, 950, 57 [5](#)
- Vázquez-Semadeni, E., Gómez, G. C., Jappsen, A. K., Ballesteros-Paredes, J., & Klessen, R. S. 2009, ApJ, 707, 1023 [2](#)
- Wang, K., Zhang, Q., Wu, Y., Li, H.-b., & Zhang, H. 2012, ApJ, 745, L30 [14](#)
- Wang, K., Zhang, Q., Testi, L., et al. 2014, MNRAS, 439, 3275 [14](#)
- Wyrowski, F., Schilke, P., Walmsley, C. M., & Menten, K. M. 1999, ApJ, 514, L43 [15](#)
- Xu, F.-W., Wang, K., Liu, T., et al. 2023a, MNRAS, 520, 3259 [2](#), [5](#)

- Xu, F., Wang, K., Liu, T., et al. 2023b, arXiv e-prints, arXiv:2309.14684 [14](#)
- Yang, D., Liu, H.-L., Tej, A., et al. 2023, ApJ, 953, 40 [2](#)
- Yuan, J., Li, J.-Z., Wu, Y., et al. 2018, ApJ, 852, 12 [2](#)
- Zhang, C., Evans, N. J., Liu, T., et al. 2022, MNRAS, 510, 4998 [5](#)
- Zhang, C., Zhu, F.-Y., Liu, T., et al. 2023a, MNRAS, 520, 3245 [5](#)
- Zhang, S., Wang, K., Liu, T., et al. 2023b, MNRAS, 520, 322 [14](#)
- Zhou, J.-W., Liu, T., Evans, N. J., et al. 2022, MNRAS, 514, 6038 [2](#), [5](#), [14](#)
- Zinnecker, H., & Yorke, H. W. 2007, ARA&A, 45, 481 [2](#)

Appendix A: SOURCE CATALOGUE

Table [A.1](#) lists all the observed targets of the QUARKS survey, including the target names, coordinates, velocity (V_{LSR}), and distance (D). For velocity and distance, both of the values adopted by the ATOMS survey (marked by a superscript of ‘old’) and the QUARKS survey (marked by a superscript of ‘new’) are listed. Table [A.2](#) lists the continuum cores of Sgr B2(M) revealed by the QUARKS survey.

Table A.1 The targets of the QUARKS survey⁽¹⁾.

ID	Target ⁽²⁾	RA (J2000)	DEC (J2000)	Glou ($^{\circ}$)	Glat ($^{\circ}$)	$V_{\text{LSR}}^{\text{old}(3)}$ (km s^{-1})	$V_{\text{LSR}}^{\text{new}}$ (km s^{-1})	D^{old} (kpc)	D^{new} (kpc)
1	I08303-4303	08:32:09.190	-43:13:44.30	261.64503	-2.08742	14.3	14.5	2.3	2.35
2	I08448-4343_1	08:46:32.270	-43:54:35.70	263.77191	-0.43510	3.7	2.8	0.7	1.22
3	I08448-4343_2	08:46:34.340	-43:54:30.50	263.77467	-0.42935	3.7	2.8	0.7	1.22
4	I08470-4243	08:48:47.720	-42:54:22.00	263.24857	+0.51455	12.0	12.1	2.1	2.27
5	I09002-4732	09:01:54.140	-47:44:09.30	268.42188	-0.84936	3.1	3.2	1.2	1.62
6	I09018-4816	09:03:32.820	-48:28:06.20	269.15212	-1.13009	10.3	9.9	2.6	2.57
7	I09094-4803	09:11:08.260	-48:15:54.60	269.85280	-0.06249	74.6	74.4	9.6	8.75
8	I10365-5803_1	10:38:32.070	-58:19:01.10	286.20619	+0.17153	-19.0	-20.1	2.4	2.49
9	I10365-5803_2	10:38:32.990	-58:19:16.70	286.21007	+0.16873	-19.0	-20.1	2.4	2.5
10	I11298-6155	11:32:06.030	-62:12:20.50	293.82778	-0.74454	32.9	33.4	10.0	9.6
11	I11332-6258	11:35:32.230	-63:14:46.80	294.51178	-1.62216	-15.4	-15.4	1.9	1.4
12	I12320-6122	12:34:53.380	-61:39:46.90	300.96916	+1.14564	-42.5	-43.2	3.43	4.17
13	I12326-6245	12:35:34.810	-63:02:32.10	301.13583	-0.22582	-39.6	-39.5	4.61	4.21
14	I12383-6128	12:41:17.320	-61:44:38.60	301.73081	+1.10402	-39.1	-39.4	3.27	4.12
15	I12572-6316_1	13:00:24.030	-63:32:31.90	303.93008	-0.68782	30.9	30.4	11.57	11.63
16	I12572-6316_2	13:00:28.730	-63:32:37.30	303.93875	-0.68962	30.9	30.4	11.57	11.63
17	I13079-6218_1	13:11:13.730	-62:34:40.20	305.20834	+0.20641	-42.6	-41.3	3.8	3.11
18	I13079-6218_2	13:11:09.500	-62:34:39.70	305.20026	+0.20717	-42.6	-41.3	3.8	3.11
19	I13080-6229	13:11:14.280	-62:44:58.30	305.19621	+0.03514	-35.6	-35.7	3.8	2.68
20	I13111-6228	13:14:26.490	-62:44:28.30	305.56239	+0.01301	-38.8	-39.5	3.8	2.97
21	I13134-6242	13:16:42.990	-62:58:29.30	305.79886	-0.24386	-31.5	-32.0	3.8	4.93
22	I13140-6226	13:17:15.900	-62:42:27.00	305.88761	+0.01594	-33.9	-34.4	3.8	4.88
23	I13291-6229_1	13:32:31.770	-62:45:11.80	307.61519	-0.25577	-36.5	-37.6	2.9	2.66
24	I13291-6229_2	13:32:34.580	-62:45:27.00	307.61981	-0.26079	-36.5	-37.6	2.9	2.66
25	I13291-6249	13:32:31.230	-63:05:21.80	307.56083	-0.58746	-34.7	-33.4	7.61	7.72
26	I13295-6152	13:32:53.490	-62:07:49.30	307.75582	+0.35251	-44.4	-44.7	3.89	3.27
27	I13471-6120	13:50:42.100	-61:35:14.90	309.92084	+0.47748	-56.7	-57.8	5.46	5.17
28	I13484-6100	13:51:58.640	-61:15:43.30	310.14416	+0.75912	-55.0	-55.3	5.4	6.64
29	I14013-6105	14:04:54.560	-61:20:10.70	311.62568	+0.28912	-48.1	-55.4	4.12	3.9
30	I14050-6056	14:08:42.150	-61:10:43.00	312.10777	+0.30909	-47.1	-47.6	3.42	3.19
31	I14164-6028	14:20:08.230	-60:42:05.00	313.57582	+0.32418	-46.5	-46.7	3.19	2.95
32	I14206-6151	14:24:22.810	-62:05:22.70	313.57583	-1.15400	-50.0	-49.7	3.29	3.19
33	I14212-6131_1	14:25:00.980	-61:44:57.50	313.76582	-0.86186	-50.5	-50.8	3.44	3.29
34	I14212-6131_2	14:25:04.240	-61:44:46.40	313.77292	-0.86125	-50.5	-50.8	3.44	3.29
35	I14382-6017	14:42:01.900	-60:30:22.50	316.13901	-0.50189	-60.7	-60.7	7.69	7.75
36	I14498-5856	14:53:42.530	-59:08:53.20	318.04937	+0.08691	-49.3	-50.2	3.16	2.99
37	I15122-5801	15:16:05.650	-58:11:39.60	321.05251	-0.50580	-60.9	-60.9	9.26	8.73
38	I15254-5621	15:29:19.480	-56:31:23.20	323.45906	-0.07914	-67.3	-68.6	4.0	4.42
39	I15290-5546	15:32:53.230	-55:56:09.60	324.20074	+0.12008	-87.5	-88.3	6.76	7.94
40	I15384-5348	15:42:17.510	-53:58:28.20	326.44810	+0.90660	-41.0	-41.1	1.82	2.41
41	I15394-5358	15:43:16.590	-54:07:14.70	326.47465	+0.70271	-41.6	-40.5	1.82	2.38
42	I15411-5352	15:44:59.460	-54:02:14.30	326.72494	+0.61576	-41.5	-41.8	1.82	2.41
43	I15437-5343	15:47:33.110	-53:52:43.90	327.11942	+0.50904	-83.0	-83.4	4.98	5.16
44	I15439-5449	15:47:49.820	-54:58:28.10	326.47310	-0.37656	-54.6	-54.8	3.29	3.4
45	I15502-5302	15:54:06.430	-53:11:38.40	328.30750	+0.43085	-91.4	-92.4	5.8	5.49
46	I15520-5234	15:55:48.390	-52:43:09.80	328.80764	+0.63243	-41.3	-41.8	2.65	2.56
47	I15522-5411_1	15:56:06.950	-54:19:58.90	327.80753	-0.63475	-46.7	-47.5	2.73	2.89
48	I15522-5411_2	15:56:08.220	-54:19:35.70	327.81403	-0.63179	-46.7	-47.5	2.73	2.89
49	I15557-5215	15:59:40.760	-52:23:27.70	329.46907	+0.50244	-67.6	-68.5	4.03	6.91
50	I15567-5236	16:00:32.860	-52:44:45.10	329.33743	+0.14749	-107.1	-107.5	5.99	5.22
51	I15570-5227	16:00:55.560	-52:36:25.20	329.47166	+0.21497	-101.5	-100.7	5.99	5.64
52	I15584-5247	16:02:19.630	-52:55:28.40	329.42299	-0.16370	-76.8	-76.4	4.41	4.87
53	I15596-5301	16:03:32.290	-53:09:28.10	329.40576	-0.45907	-72.1	-73.7	10.11	9.2
54	I16026-5035_1	16:06:25.630	-50:43:18.10	331.35920	+1.06314	-78.3	-79.0	4.53	5.05
55	I16026-5035_2	16:06:23.110	-50:43:26.10	331.35277	+1.06593	-78.3	-79.0	4.53	5.05

⁽¹⁾ This table contains 156 rows.⁽²⁾ The two pointing targets associated with a same source were denoted by suffixes “_1” and “_2”.⁽³⁾ The V_{LSR} is the velocity revealed by surveys before the ATOMS survey. The $V_{\text{LSR}}^{\text{new}}$ is the velocity revealed by the H^{13}CO^+ data of the ATOMS survey. The D^{old} is the distance adopted by the ATOMS survey, originally derived from the Galactic rotation curve by Bronfman et al. (1996). The D^{new} is derived from the coordinate and $V_{\text{LSR}}^{\text{new}}$, using the distance calculator of Reid et al. (2016). See Section 2.1 for details.

Table A.1 continued.

ID	Target	RA (J2000)	DEC (J2000)	Glou ($^{\circ}$)	Glat ($^{\circ}$)	$V_{\text{LSR}}^{\text{old}}$ (km s^{-1})	$V_{\text{LSR}}^{\text{new}}$ (km s^{-1})	D^{old} (kpc)	D^{new} (kpc)
56	I16037-5223	16:07:38.100	-52:31:00.20	330.29433	-0.39406	-80.0	-81.3	9.84	9.04
57	I16060-5146	16:09:52.850	-51:54:54.70	330.95419	-0.18248	-91.6	-92.1	5.3	5.39
58	I16065-5158	16:10:19.600	-52:06:07.10	330.87788	-0.36624	-63.3	-62.5	3.98	4.33
59	I16071-5142	16:10:59.010	-51:50:21.60	331.13062	-0.24240	-87.0	-86.5	5.3	5.29
60	I16076-5134	16:11:27.120	-51:41:56.90	331.27918	-0.18915	-87.7	-87.8	5.3	5.31
61	I16119-5048	16:15:45.650	-50:55:58.50	332.29482	-0.09513	-48.2	-48.6	3.1	3.42
62	I16132-5039_1	16:17:01.920	-50:46:51.00	332.54480	-0.12485	-47.5	-47.6	3.1	3.36
63	I16132-5039_2	16:17:02.690	-50:47:07.10	332.54315	-0.12947	-47.5	-47.6	3.1	3.36
64	I16164-5046	16:20:10.910	-50:53:15.50	332.82560	-0.54900	-57.3	-56.7	3.57	4.02
65	I16172-5028_1	16:21:02.930	-50:35:11.60	333.13502	-0.43180	-51.9	-53.3	3.57	3.78
66	I16172-5028_2	16:21:00.160	-50:35:09.10	333.13032	-0.42614	-51.9	-53.3	3.57	3.79
67	I16177-5018	16:21:31.490	-50:25:04.50	333.30767	-0.36574	-50.2	-50.0	3.57	3.53
68	I16272-4837	16:30:58.020	-48:43:46.60	335.58505	-0.28737	-46.6	-46.8	2.92	3.54
69	I16297-4757	16:33:29.290	-48:03:31.50	336.36099	-0.13529	-79.6	-79.3	5.03	5.1
70	I16304-4710	16:34:04.800	-47:16:32.00	337.00368	+0.32327	-62.8	-62.3	11.32	10.5
71	I16313-4729	16:34:55.440	-47:35:40.90	336.86551	+0.00213	-73.7	-74.1	4.71	4.99
72	I16318-4724	16:35:33.200	-47:31:11.30	336.99245	-0.02558	-119.8	-120.8	7.68	7.95
73	I16330-4725	16:36:42.600	-47:31:30.80	337.11993	-0.17360	-75.1	-75.4	10.99	9.96
74	I16344-4658	16:38:10.380	-47:04:56.70	337.61479	-0.06089	-49.5	-49.7	12.09	11.23
75	I16348-4654	16:38:29.420	-47:00:39.70	337.70403	-0.05342	-46.5	-47.8	12.09	11.33
76	I16351-4722	16:38:50.610	-47:27:59.70	337.40474	-0.40206	-41.4	-40.8	3.02	2.33
77	I16362-4639	16:39:57.700	-46:45:04.30	338.06530	-0.06792	-38.8	-38.6	3.01	2.26
78	I16372-4545	16:40:54.770	-45:50:53.60	338.85013	+0.40789	-57.3	-57.5	4.16	4.42
79	I16385-4619	16:42:13.980	-46:25:27.20	338.56865	-0.14425	-117.0	-117.0	7.11	5.76
80	I16424-4531	16:46:06.610	-45:36:46.60	339.62257	-0.12249	-34.2	-34.5	2.63	2.19
81	I16445-4459	16:48:05.180	-45:05:08.60	340.24917	-0.04582	-121.3	-122.2	7.95	7.72
82	I16458-4512	16:49:30.410	-45:17:53.60	340.24749	-0.37413	-50.4	-50.9	3.56	4.19
83	I16484-4603	16:52:03.990	-46:08:24.60	339.88482	-1.25558	-32.0	-32.4	2.1	2.17
84	I16487-4423_1	16:52:23.670	-44:27:52.30	341.21578	-0.23579	-43.4	-44.0	3.26	2.65
85	I16487-4423_2	16:52:21.590	-44:28:00.60	341.21007	-0.23248	-43.4	-44.0	3.26	2.65
86	I16489-4431	16:52:34.080	-44:36:16.70	341.12713	-0.34861	-41.3	-41.1	3.26	2.48
87	I16524-4300	16:56:03.060	-43:04:47.30	342.70669	+0.12514	-40.8	-40.6	3.43	2.52
88	I16547-4247	16:58:17.260	-42:52:04.50	343.12750	-0.06248	-30.4	-30.6	2.74	2.19
89	I16562-3959	16:59:41.450	-40:03:34.60	345.49528	+1.47062	-12.6	-11.3	2.38	1.37
90	I16571-4029	17:00:32.380	-40:34:13.80	345.19280	+1.02820	-15.0	-15.4	2.38	2.13
91	I17006-4215	17:04:13.200	-42:19:54.20	344.22119	-0.59458	-23.2	-24.3	2.21	2.85
92	I17008-4040	17:04:23.200	-40:44:24.90	345.50460	+0.34705	-17.0	-17.3	2.38	1.33
93	I17016-4124	17:05:11.020	-41:29:07.80	345.00285	-0.22408	-27.1	-26.8	1.37	3.16
94	I17136-3617	17:17:02.290	-36:21:02.10	350.50570	+0.95672	-10.6	-11.6	1.34	1.33
95	I17143-3700	17:17:45.650	-37:03:11.80	350.01583	+0.43248	-31.1	-31.7	12.67	11.71
96	I17158-3901	17:19:20.340	-39:03:53.30	348.54925	-0.97890	-15.2	-16.6	3.38	3.33
97	I17160-3707	17:19:27.310	-37:11:00.40	350.10365	+0.08132	-69.5	-69.4	10.53	10.28
98	I17175-3544	17:20:53.570	-35:46:59.80	351.41758	+0.64492	-5.7	-8.7	1.34	1.32
99	I17204-3636	17:23:50.320	-36:38:58.10	351.04114	-0.33570	-18.2	-18.1	3.32	3.27
100	I17220-3609	17:25:24.990	-36:12:41.10	351.58185	-0.35181	-93.7	-97.2	8.01	8.05
101	I17233-3606	17:26:42.800	-36:09:16.80	351.77525	-0.53699	-2.7	-3.1	1.34	1.32
102	I17244-3536	17:27:48.710	-35:39:10.80	352.31584	-0.44245	-10.2	-10.8	1.36	2.63
103	I17258-3637	17:29:17.130	-36:40:12.60	351.63374	-1.25360	-11.9	-10.5	2.59	1.33
104	I17269-3312_1	17:30:15.200	-33:14:57.50	354.59672	+0.46787	-21.0	-21.4	4.38	4.53
105	I17269-3312_2	17:30:14.120	-33:14:22.60	354.60274	+0.47635	-21.0	-21.4	4.38	4.53
106	I17271-3439_1	17:30:26.210	-34:41:45.40	353.40990	-0.36021	-18.2	-17.2	3.1	3.66
107	I17271-3439_2	17:30:27.710	-34:41:45.90	353.41261	-0.36457	-18.2	-17.2	3.1	3.67
108	I17278-3541	17:31:14.070	-35:44:04.30	352.63152	-1.06690	-0.4	-0.5	1.33	1.32
109	I17439-2845_1	17:47:09.060	-28:46:17.80	0.31480	-0.20090	18.7	18.4	8.0	6.93
110	I17439-2845_2	17:47:07.190	-28:46:01.30	0.31518	-0.19269	18.7	18.4	8.0	6.94
111	I17441-2822	17:47:19.790	-28:23:05.70	0.66589	-0.03412	50.8	50.8	8.1	8.3
112	I17455-2800	17:48:41.630	-28:01:44.60	1.12584	-0.10749	-15.6	-14.8	10.0	11.14
113	I17545-2357	17:57:34.490	-23:58:04.30	5.63735	+0.23748	7.9	8.8	2.93	3.0
114	I17589-2312	18:01:58.000	-23:12:32.00	6.79633	-0.25777	21.3	20.5	2.97	3.44
115	I17599-2148	18:03:01.470	-21:48:06.30	8.14078	+0.22409	18.6	18.6	2.99	3.44
116	I18032-2032	18:06:14.300	-20:31:35.00	9.61969	+0.19657	4.3	4.4	5.15	4.8
117	I18056-1952	18:08:38.180	-19:51:49.00	10.47249	+0.02752	66.7	66.4	8.55	8.44
118	I18075-2040	18:10:34.500	-20:39:16.10	10.00023	-0.75297	31.5	31.2	3.08	2.8
119	I18079-1756	18:10:50.770	-17:55:45.20	12.41844	+0.50544	18.0	17.8	1.83	2.32
120	I18089-1732	18:11:51.060	-17:31:27.20	12.88863	+0.49074	33.5	32.9	2.5	3.64

Table A.1 continued.

ID	Target	RA (J2000)	DEC (J2000)	Glou ($^{\circ}$)	Glat ($^{\circ}$)	$V_{\text{LSR}}^{\text{old}}$ (km s^{-1})	$V_{\text{LSR}}^{\text{new}}$ (km s^{-1})	D^{old} (kpc)	D^{new} (kpc)
121	I18110-1854	18:14:01.050	-18:53:23.30	11.93713	-0.61570	37.0	38.5	3.37	3.17
122	I18116-1646	18:14:35.960	-16:45:36.80	13.87386	+0.28067	48.5	48.8	3.94	3.86
123	I18117-1753	18:14:39.250	-17:51:59.80	12.90811	-0.25932	36.7	37.1	2.57	3.63
124	I18134-1942	18:16:22.120	-19:41:27.00	11.49742	-1.48527	10.6	10.5	1.25	1.25
125	I18139-1842	18:16:51.590	-18:41:34.70	12.43083	-1.11328	39.8	39.8	3.02	3.0
126	I18159-1648	18:18:54.340	-16:47:45.90	14.33225	-0.64324	22.0	22.4	1.48	2.83
127	I18182-1433	18:21:09.220	-14:31:46.80	16.58584	-0.05082	59.1	59.3	4.71	3.66
128	I18223-1243	18:25:10.580	-12:42:22.20	18.65473	-0.05887	44.8	45.0	3.37	3.46
129	I18228-1312	18:25:42.270	-13:10:17.00	18.30343	-0.38990	32.3	32.8	3.21	3.2
130	I18236-1205	18:26:25.650	-12:03:57.60	19.36348	-0.03031	25.9	26.1	2.17	2.88
131	I18264-1152	18:29:14.500	-11:50:19.50	19.88476	-0.53396	43.2	43.6	3.33	3.35
132	I18290-0924_1	18:31:42.980	-09:22:26.00	22.35097	+0.06876	84.2	84.0	5.34	4.69
133	I18290-0924_2	18:31:43.740	-09:22:19.00	22.35413	+0.06689	84.2	84.0	5.34	4.69
134	I18308-0503_1	18:33:29.780	-05:01:04.30	26.41961	+1.68770	42.9	42.6	3.1	3.75
135	I18308-0503_2	18:33:30.850	-05:00:58.70	26.42303	+1.68447	42.9	42.6	3.1	3.75
136	I18311-0809	18:33:53.430	-08:07:14.40	23.71065	+0.17082	113.0	112.9	6.06	6.27
137	I18314-0720_1	18:34:10.010	-07:18:00.30	24.47044	+0.48830	101.5	101.3	5.82	6.15
138	I18314-0720_2	18:34:09.050	-07:17:50.80	24.47095	+0.49303	101.5	101.3	5.82	6.15
139	I18316-0602	18:34:20.580	-05:59:41.60	25.64915	+1.05073	42.8	42.7	2.09	3.76
140	I18317-0513	18:34:25.800	-05:10:53.50	26.38134	+1.40596	42.1	41.8	2.18	3.73
141	I18317-0757	18:34:24.900	-07:54:47.60	23.95460	+0.15119	80.7	81.2	4.79	4.7
142	I18341-0727	18:36:50.400	-07:24:48.00	24.67487	-0.15227	112.7	113.1	6.04	6.39
143	I18411-0338	18:43:46.260	-03:35:23.90	28.86343	+0.06630	102.8	103.5	7.41	5.46
144	I18434-0242	18:46:04.200	-02:39:18.30	29.95723	-0.01729	97.2	97.5	5.16	4.76
145	I18440-0148	18:46:36.390	-01:45:22.00	30.81828	+0.27376	97.5	97.6	5.16	6.04
146	I18445-0222	18:47:09.760	-02:18:47.60	30.38596	-0.10410	86.9	86.6	5.16	6.24
147	I18461-0113	18:48:42.230	-01:10:05.40	31.58061	+0.07556	96.1	96.0	5.16	5.67
148	I18469-0132	18:49:33.150	-01:29:06.20	31.39533	-0.25773	87.0	86.6	5.16	4.91
149	I18479-0005	18:50:31.200	-00:01:56.00	32.79860	+0.18954	14.6	14.6	12.96	12.87
150	I18507+0110	18:53:18.120	+01:15:00.10	34.25691	+0.15530	57.2	58.2	1.56	3.23
151	I18507+0121	18:53:18.150	+01:25:22.40	34.41081	+0.23402	57.9	57.8	1.56	3.09
152	I18517+0437	18:54:14.110	+04:41:43.10	37.43000	+1.51849	43.9	43.9	2.36	2.36
153	I18530+0215	18:55:33.610	+02:19:09.00	35.46573	+0.14083	74.1	76.9	4.67	5.08
154	I19078+0901	19:10:13.410	+09:06:10.40	43.16581	+0.01086	2.9	6.2	11.11	11.49
155	I19095+0930	19:11:53.900	+09:35:45.90	43.79414	-0.12749	43.7	43.8	6.02	9.07
156	I19097+0847	19:12:08.900	+08:52:07.80	43.17804	-0.51881	58.0	58.2	8.47	7.83

Table A.2 The continuum cores in Sgr B2(M) detected by the QUARKS survey ⁽¹⁾.

Core ID	RA (J2000) ($^{\circ}$)	DEC (J2000) ($^{\circ}$)	L_{\max} ($''$)	L_{\min} ($''$)	PA ⁽²⁾ ($^{\circ}$)	$I_{\text{peak}}^{(3)}$ (Jy beam $^{-1}$)	Flux ⁽⁴⁾ Jy	SM17 ⁽⁵⁾
1	266.83403	-28.38466	0.9	0.7	-60.0	1.2384	2.9881(33)	Y
2	266.83390	-28.38451	0.7	0.5	-48.0	1.0232	1.6362(19)	Y
3	266.83377	-28.38439	0.5	0.5	0.0	0.4462	0.5199(7)	N
4	266.83421	-28.38456	0.6	0.5	0.0	0.4320	0.4593(7)	N
5	266.83379	-28.38418	0.6	0.5	0.0	0.2037	0.3029(5)	Y
6	266.83393	-28.38489	0.7	0.6	0.0	0.3453	0.8302(11)	Y
7	266.83409	-28.38502	0.6	0.5	0.0	0.3427	0.4357(5)	Y
8	266.83362	-28.38459	0.8	0.6	-30.0	0.2454	0.3665(5)	N
9	266.83383	-28.38510	0.6	0.6	-51.0	0.2598	0.4426(7)	Y
10	266.83416	-28.38520	0.6	0.5	34.0	0.1956	0.3105(5)	Y
11	266.83433	-28.38535	0.6	0.5	39.0	0.1103	0.1880(4)	Y
12	266.83405	-28.38436	0.6	0.4	-6.0	0.3207	0.3038(5)	N
13	266.83394	-28.38397	0.7	0.5	0.0	0.0739	0.1490(4)	Y
14	266.83454	-28.38421	0.6	0.6	0.0	0.2274	0.2956(5)	Y
15	266.83449	-28.38438	0.6	0.4	0.0	0.0627	0.0839(2)	Y
16	266.83413	-28.38421	1.0	0.6	0.0	0.1171	0.3160(5)	N
17	266.83379	-28.38378	1.0	0.5	41.0	0.0500	0.1045(4)	N
18	266.83300	-28.38415	0.9	0.5	90.0	0.0638	0.1336(4)	Y
19	266.83359	-28.38506	0.7	0.5	21.0	0.0984	0.2074(4)	Y
20	266.83336	-28.38496	0.7	0.5	26.0	0.0696	0.1301(4)	N
21	266.83314	-28.38486	0.7	0.5	15.0	0.0654	0.1284(4)	Y
22	266.83292	-28.38476	0.8	0.5	23.0	0.0526	0.1140(4)	N
23	266.83264	-28.38459	0.9	0.8	0.0	0.0295	0.0910(4)	N
24	266.83237	-28.38441	0.8	0.7	0.0	0.0178	0.0388(2)	N
25	266.83349	-28.38527	1.1	0.8	-65.0	0.0678	0.3022(7)	N
26	266.83289	-28.38519	0.4	0.4	0.0	0.0213	0.0187(2)	N
27	266.83380	-28.38579	0.9	0.6	-69.0	0.0520	0.1187(4)	Y
28	266.83304	-28.38608	0.6	0.5	0.0	0.0360	0.0467(2)	Y
29	266.83297	-28.38591	0.6	0.6	0.0	0.0239	0.0449(2)	N
30	266.83306	-28.38560	0.7	0.6	0.0	0.0154	0.0369(2)	N
31	266.83315	-28.38632	1.3	1.1	90.0	0.0190	0.1026(5)	N
32	266.83340	-28.38643	0.6	0.5	-57.0	0.0118	0.0161(2)	N
33	266.83272	-28.38625	0.7	0.5	0.0	0.0132	0.0193(2)	N
34	266.83359	-28.38693	1.0	0.9	90.0	0.0171	0.0588(4)	N
35	266.83378	-28.38710	0.7	0.6	40.0	0.0074	0.0160(2)	N
36	266.83372	-28.38732	0.6	0.6	0.0	0.0055	0.0081(2)	N
37	266.83435	-28.38749	0.7	0.5	0.0	0.0046	0.0013(2)	N
38	266.83228	-28.38615	0.8	0.6	9.0	0.0234	0.0583(2)	N
39	266.83207	-28.38595	0.6	0.5	38.0	0.0415	0.0597(2)	N
40	266.83204	-28.38580	0.5	0.4	90.0	0.0262	0.0285(2)	Y
41	266.83175	-28.38563	0.7	0.6	0.0	0.1086	0.1925(4)	Y
42	266.83192	-28.38617	0.6	0.4	0.0	0.0207	0.0313(2)	N
43	266.83193	-28.38633	0.6	0.5	0.0	0.0270	0.0367(2)	N
44	266.83154	-28.38575	0.5	0.4	0.0	0.0245	0.0313(2)	N
45	266.83151	-28.38605	0.8	0.7	90.0	0.0166	0.0451(2)	N
46	266.83192	-28.38652	0.8	0.6	-8.0	0.0098	0.0205(2)	N
47	266.83210	-28.38535	0.7	0.6	0.0	0.0284	0.0473(2)	Y
48	266.83159	-28.38530	0.6	0.4	-39.0	0.0382	0.0480(2)	Y
49	266.83166	-28.38539	0.4	0.3	0.0	0.0288	0.0217(2)	N
50	266.83135	-28.38516	0.9	0.5	53.0	0.0124	0.0259(2)	N
51	266.83111	-28.38526	0.6	0.4	0.0	0.0162	0.0165(2)	N
52	266.83100	-28.38547	0.7	0.4	25.0	0.0474	0.0584(2)	Y
53	266.83088	-28.38555	0.5	0.5	0.0	0.0251	0.0303(2)	N
54	266.83062	-28.38583	0.9	0.6	0.0	0.0226	0.0458(2)	Y
55	266.83109	-28.38703	0.6	0.6	0.0	0.0081	0.0059(2)	N

⁽¹⁾ This table contains 97 rows.⁽²⁾ The position angle (PA) is defined in the style of DS9. When PA is 0° , the major axis is in the direction of east. The major axis rotates from the east to the north when PA changes from 0° to 90° .⁽³⁾ The uncertainty of the I_{peak} is estimated to be 1 mJy beam^{-1} for weak cores.⁽⁴⁾ The number in the bracket is the uncertainty of the last digital of the flux.⁽⁵⁾ Denote if the corresponding core has been identified by [Sánchez-Monge et al. \(2017\)](#).

Table A.2 continued.

Core ID	RA (J2000) ($^{\circ}$)	DEC (J2000) ($^{\circ}$)	L_{\max} ($''$)	L_{\min} ($''$)	PA ($^{\circ}$)	I_{peak} (Jy beam $^{-1}$)	Flux Jy	SM17
56	266.83333	-28.38848	1.1	1.1	90.0	0.0100	0.0320(5)	N
57	266.83148	-28.38423	0.6	0.5	0.0	0.0453	0.0664(2)	Y
58	266.83151	-28.38408	0.4	0.4	90.0	0.0274	0.0228(2)	N
59	266.83118	-28.38441	0.5	0.5	0.0	0.0154	0.0154(2)	N
60	266.83079	-28.38422	0.6	0.4	30.0	0.0231	0.0289(2)	Y
61	266.83172	-28.38373	1.1	0.6	0.0	0.0063	0.0150(2)	N
62	266.83121	-28.38339	0.5	0.5	0.0	0.0165	0.0174(2)	N
63	266.83107	-28.38326	0.7	0.7	0.0	0.0221	0.0492(2)	Y
64	266.83085	-28.38320	0.7	0.5	0.0	0.0137	0.0212(2)	N
65	266.83039	-28.38351	1.6	1.1	-51.0	0.0067	0.0416(5)	N
66	266.83007	-28.38412	0.5	0.4	0.0	0.0128	0.0106(2)	N
67	266.82988	-28.38406	0.4	0.4	-55.0	0.0089	0.0079(2)	N
68	266.82947	-28.38455	0.8	0.7	-31.0	0.0281	0.0585(2)	N
69	266.82931	-28.38468	0.5	0.5	0.0	0.0082	0.0077(2)	N
70	266.82923	-28.38447	0.7	0.6	0.0	0.0102	0.0193(2)	N
71	266.82954	-28.38401	0.9	0.7	90.0	0.0096	0.0296(2)	N
72	266.82939	-28.38363	0.5	0.4	0.0	0.0072	0.0063(2)	N
73	266.82919	-28.38513	0.6	0.5	72.0	0.0087	0.0122(2)	N
74	266.82901	-28.38517	0.5	0.4	0.0	0.0126	0.0114(2)	N
75	266.82871	-28.38522	0.8	0.4	-25.0	0.0107	0.0172(2)	N
76	266.82813	-28.38442	0.6	0.6	0.0	0.0399	0.0576(2)	N
77	266.82837	-28.38439	0.5	0.5	0.0	0.0165	0.0187(2)	N
78	266.82810	-28.38234	1.2	0.8	0.0	0.0306	0.1156(5)	N
79	266.83354	-28.38364	0.8	0.5	0.0	0.0173	0.0367(2)	N
80	266.83329	-28.38363	0.7	0.7	0.0	0.0099	0.0236(2)	N
81	266.83333	-28.38305	1.1	0.9	0.0	0.0056	0.0184(4)	N
82	266.83360	-28.38299	1.1	0.7	90.0	0.0055	0.0136(4)	N
83	266.83382	-28.38290	0.8	0.7	0.0	0.0057	0.0132(2)	N
84	266.83417	-28.38275	1.0	0.9	90.0	0.0074	0.0256(4)	N
85	266.83135	-28.38218	1.1	0.9	90.0	0.0054	0.0133(4)	N
86	266.82855	-28.38578	0.7	0.6	0.0	0.0115	0.0181(2)	N
87	266.83417	-28.38583	0.9	0.8	90.0	0.0169	0.0597(4)	N
88	266.83468	-28.38563	0.5	0.5	90.0	0.0233	0.0276(2)	N
89	266.83469	-28.38546	0.6	0.5	15.0	0.0254	0.0431(2)	N
90	266.83490	-28.38548	0.8	0.7	0.0	0.0219	0.0679(4)	Y
91	266.83485	-28.38524	0.9	0.8	90.0	0.0239	0.0998(4)	N
92	266.83496	-28.38479	1.5	1.0	-50.0	0.0580	0.3959(9)	Y
93	266.83539	-28.38452	1.8	0.9	0.0	0.0358	0.2894(8)	N
94	266.83504	-28.38655	1.9	1.8	0.0	0.0067	0.0579(8)	N
95	266.83296	-28.38263	1.5	1.1	-56.0	0.0037	0.0067(5)	N
96	266.83133	-28.38798	0.6	0.5	-30.0	0.0052	0.0062(2)	N
97	266.83254	-28.38526	0.5	0.5	0.0	0.0043	0.0053(2)	N